J Garcia et al.

Physics comparison and modelling of the JET and JT-60U core and edge: towards JT-60SA predictions

Physics Comparison and Modelling of the JET and JT-60U Core and Edge: Towards JT-60SA Predictions

J. Garcia[1], N. Hayashi[2], B. Baiocchi[1], G. Giruzzi[1], M. Honda[2], S. Ide[2], P. Maget[1],
E. Narita[3], M. Schneider[1], H. Urano[2], the JT-60U Team,
the EU-ITM ITER Scenario Modelling Group and JET EFDA contributors*

JET-EFDA, Culham Science Centre, OX14 3DB, Abingdon, UK

[1]*CEA, IRFM, 13108 Saint-Paul-lez-Durance, France*
[2]*Japan Atomic Energy Agency, Mukouyama, Naka, Ibaraki, 311-0193 Japan*
[3]*Osaka University, Yamadaoka, Suita 565-0871, Japan*
* *See annex of F. Romanelli et al, "Overview of JET Results",*
(24th IAEA Fusion Energy Conference, San Diego, USA (2012)).

ABSTRACT

Extensive physics analysis and modeling has been undertaken for the typical operational regimes of the tokamak devices JET and JT-60U with the aim of extrapolating present day experiments to JT-60SA, which shares important characteristics with both tokamaks. A series of representative discharges of two operational scenarios, H-mode and hybrid, have been used for this purpose. Predictive simulations of core turbulence, particle transport, current diffusion and pedestal pressure have been carried out with different combinations of models. The ability of the models for reproducing the experimental data is analyzed and scenario calculations for JT-60SA are performed following an optimum set of models.

1. INTRODUCTION

In the framework of the construction of new tokamaks, such as JT-60SA, ITER and DEMO, the necessity of predicting the performance of the main operation scenarios has been identified as a main goal, both for the detailed definition of the properties of various machine subsystems (heating and current drive, control coils, diagnostics) and in order to establish a reliable starting point for plasma operation.

For this purpose, validation of the main models available for the plasma simulation is mandatory. These include, e.g., energy and particle transport, current, rotation and their sources, pedestal pressure and fast particles. JT-60SA [1] is a machine designed on the basis of the results of JT-60U, and using an upgrade of the JT-60U Neutral Beam Injection (NBI) system; on the other hand, it has practically the same size as JET, which also has NBI as the main heating and current drive system. Therefore, it appears that simulations of JT-60SA scenarios should be based at least on experimental results of the two machines that are the most similar, for size and configuration: JT-60U and JET. On this basis, an extensive validation exercise has been undertaken with the aim, as well, of expanding the knowledge of these models towards more realistic simulation of future tokamak devices such as ITER and DEMO.

For this purpose, in the framework of a broad research plan based on JT-60SA [1], a series of representative discharges of the three main operational scenarios, H-mode, hybrid and steady-state, have been selected for each device. A subset of these discharges, inductive H-modes and hybrids are discussed in this paper. Their main parameters can be found in Table I. The selected time for the analysis concentrates on the phase of highest performance of each of these discharges.

The work has been divided in several stages. First, an analysis of the physics involved in the core and at the edge has been carried out with the aim of understanding the possible success or failure of the models applied. Then, predictive simulations for the temperature profiles have been carried out with three transport models, Bohm-GyroBohm [2], CDBM [3] and GLF23 [4], and by adjusting, as a first step, the pedestal, rotation and density to experimental values whenever available. To carry out this programme, the integrated modelling codes CRONOS [5] and TOPICS [6] have been used in order to benchmark the models in both codes. Finally, fully predictive

simulations of temperatures, density and pedestal have been performed. In the case of the pedestal, the density at the edge is forced to follow neoclassical transport, whereas the pedestal temperature is calculated by using the so-called Cordey two-term scaling [7]. With this approach, calculations for JT-60SA have been carried out.

The paper is organized as follows. In section 2 the core and edge physics analysis is shown for selected JET and JT-60U discharges. In section 3 the results of predictive simulations of the temperatures are compared with the experimental data. In section 3, analysis and simulation of particle transport for both devices will be shown. In section 5, fully self- consistent simulations of current density, heat and particle transport and pedestal pressure are presented and discussed. The statistical analysis of the performance of the models applied in here will be also carried out in this section.Finally, in section 6, simulations for two JT-60SA scenarios, inductive H-mode and hybrid, are shown as a demonstration of the validated modelling framework. Conclusions are drawn in section 7.

2. PHYSICS ANALYSIS

Linear gyrokinetic analysis has been performed with the GENE [8] code for the JET discharges 73344 and 75225 [9] and for the JT-60U discharges 33654 and 48158 [10]. For the gyrokinetic analysis of the discharges, all simulations included kinetic electrons, collisions, and electromagnetic effects. The geometry used was calculated by the equilibrium code HELENA [11] on the basis of the interpretative analyses of the discharges. The turbulent linear growth rates γ are in units of c_s/R, with $c_s = \sqrt{T_e/m_i}$ and m_i the main ion mass. In these electromagnetic simulations, both $\delta B_\perp$ and $\delta B_\parallel$ fluctuations were computed, as they can play a significant role in high β discharges [12].The selected time for the JET discharge 75225 is t = 6.03s, in which the performance is maximized and no core MHD is detected and at t = 27s for the JT-60U discharge 48158. For the inductive H-modes discharges the time is t = 9.2s for JET 73344 and t = 8.0s for JT-60U 33654. The region for the scan is around $\rho = 0.33$ (where ρ is the normalized radius, defined from the toroidal flux), as it is a point representative of the core turbulence for hybrid scenarios in which no significant sawteeth activity is found. For the inductive H-mode scenarios, $\rho = 0.5$ is chosen, as the inner core region is dominated by MHD activity. Only thermal species have been taken into account in these simulations.

As shown in figure 1, for the inductive H-mode discharges, the turbulence is dominated by the Ion Temperature Gradient (ITG) instability [13] for the full perpendicular wave number ky, as expected from this low beta discharges. On the other hand, for the hybrid discharges, some differences are found. For the JET 75225 discharge, as shown in figure 2, ITG dominates for the full spectrum. However, the spectrum for the JT-60U 48158 discharge is dominated by the Trapped Electron Mode (TEM) regime for ky > 0.3 where the modes drift in the electron diamagnetic direction, likely due to the high normalized density gradient, $L_{ne} = -Rn_n/\nabla n_e \approx 5$, much higher than in the JET case, $L_{ne} \approx 1.5$, and which is known to drive this type of instability [14]. The different turbulence regime can have an impact on the results of predictive heat transport simulations, as transport models

2

usually have difficulties for reproducing temperatures in such regimes [15]. This point will be further analyzed in the following sections. For ky ≤ 0.3, the JT-60U shot 48158 also has modes drifting in the ion diamagnetic frequency but with higher frequency than ITG and which can be a manifestation of Kinetic Ballooning Modes (KBM) although further analyses must be carried out in order to verify this point.

The peeling-ballooning stability analysis of the hybrid discharges JET 75225 and JT-60U 48158 have been also carried out in order to validate whether the assumptions for the pressure pedestal assumed in section 6 for the JT-60SA tokamak, based on JET and JT-60U data, can be verified using this theory. For this purpose the code MISHKA [16] and the procedure described in [17] are used. In figure 3 the stability boundary and the pressure pedestal are shown. For both discharges, the experimental pressure lies at the ballooning region of the stable part of the diagram.

3. HEAT TRANSPORT PREDICTIVE SIMULATION

Predictive simulations of the temperature profiles have been carried out with the transport modelsBohm-GyroBohm, CDBM and GLF23with the codes CRONOS and TOPICS. The NBI current drive and fast ion pressure has been calculated with the Monte Carlo codes NEMO/SPOT [18,19] for JET discharges and OMFC [20] for the JT-60U discharges. In these simulations, the pedestal temperature and density have been fixed to experimental values.

Regarding the CDBM transport model, a modification has been implemented in order to take into account the relatively high fast ion population in some of the discharges, mainly hybrid ones. For that purpose, the fast ion pressure is included in the normalized pressure gradient $\alpha = -Rq^2 d\beta/dr$, with R major radius, r minor radius, q safety factor, $\beta = 2\mu_0 <P>/B^2$ with $<P>$ the volume averaged pressure and B the magnetic field which is taken into account in the function

$$F(s,\alpha) = \begin{cases} \dfrac{1}{\sqrt{2(1-2s')(1-2s'+3s'^2)}}, & for \ \ s'=s-\alpha < 0 \\ \dfrac{(1+9\sqrt{2}s'^{5/2})}{\sqrt{2}(1-2s'+3s'^2+2s'^3)}, & for \ \ s'=s-\alpha > 0 \end{cases} \tag{1}$$

where s is the magnetic shear. The thermal pressure gradient $\alpha_{th} = -Rq^2 d\beta/dr$, only including the thermal pressure, is used in the other terms. The original heat diffusivities [3] are mended as follows:

$$\chi_{CDBM} = 12\frac{c^2}{\omega_{pe}^2}\frac{v_A}{qR}\alpha_{th}^{3/2}F(s,\alpha)G(\kappa) \ and \ G(\kappa)=(2\kappa^{1/2}/(\kappa^2+1))^{3/2}$$

with κ the elongation, ω_{pe} the electron plasma frequency and v_A is the toroidalAlfvén velocity.

The q and density profiles for each of the discharges at the time considered are shown in figure 4 and figure 5 for the inductive H-modes and hybrids respectively. For the ExB shearing rate γ_{ExB}, the standard multiplier $\alpha_{ExB} = 1.35$ has been used throughout this study when GLF23 transport model has been applied. The experimental measured rotation has been always taken as a boundary condition.

The predictive results for the inductive scenarios are shown in figures 6 and 7. In general, the agreement between both codes and with experimental data for the inductive H-modes is acceptable, in particular for the GLF23 transport model. Except for the electron temperature of the JT-60U discharge 33654, which is lower than the experimental data, GLF23 gives reasonable results for the other temperature profiles. On the other hand, the CDBM transport model is quite close to GLF23 results although it tends to give somewhat lower temperatures. This is particularly clear for the JET discharges. Finally, the Bohm-GyroBohm model is accurate for the JET discharges but with more scattered results for the JT-60U ones. Therefore, none of the models give equally accurate results for all the discharges analyzed, but the predictions remain within reasonable agreement, as will be shown in section 5. It is important to stress that no sawtooth model has been used for the simulation of these discharges and thus the predictions in the central region, which is likely to be affected by sawteeth, must be taken with care.

Predictive simulations of hybrid discharges have been also carried out. In figure 8 the simulation of the JT-60U discharge 48158 is shown whereas the JET discharges are shown in figure 9. The general agreement between TOPICS and CRONOS for hybrid scenarios is not as good as for the inductive H-mode regimes, mainly for the ion channel. The reasons are slightly differences in the magnetic equilibrium and neoclassical transport which are particularly important in this regime where a significant fraction of anomalous transport is quenched by different physical mechanisms, as the ExB flow.

For this scenario, the Bohm-GyroBohm transport model tends to overestimate temperatures, even for JET, and mainly for ions. On the other hand, CDBM gives results closer to experimental data, mainly for the ions. Finally, as expected from other analyses of the same kind [21], the GLF23 transport model tends to overestimate the ion temperature whereas it gives correct results for the electron temperature. The reason for this is likely the too strong impact of rotation on these discharges through the ExB shearing rate. In order to explore this possibility, the same simulations have been carried out with CRONOS by setting $\alpha_{ExB} = 0$. The ion temperatures, shown in figure 10, clearly drop and get close to experimental ones in the case of JET. However, for the JT-60U discharge, a region of flat temperature appears in $0.2 < \rho < 0.5$ which makes this new calculation much lower than reality. This behavior can be explained by the existence of TEM modes in that region, as pointed out in section 2, for which GLF23 overestimates heat transport. A more suited transport model for that regime would be TGLF, which has been specially created for dealing with these modes [22].

In the case of the CDBM model, the different treatment of thermal and fast ions pressure leads to better results than the original model. In figure 11, the electron and ion temperatures for the JT-60SA 48158 discharge with the original model and the amended one are shown. The profiles obtained with the new version are closer to experimental data, something especially important for ions.

In conclusion, whereas for inductive H-modes, the models considered do not largely deviate from experimental data, mainly with GLF23, the situation for hybrids tends to be more scattered,

4

with a clear overestimation of ion temperatures because of the too strong impact of rotation on GLF23, which makes the prediction by CDBM more suitable. This has important implications for the extrapolation to JT-60SA, as will be shown in the following sections. The overall statistical analysis of the predictive simulations will be shown in section 5.

4. PARTICLE TRANSPORT ANALYSIS

Particle transport has been also analysed by performing simultaneous predictions of ion and electron temperature profiles and electron density. Since it has been shown in the previous section that the GLF23 transport model is able to properly reproduce inductive H-mode scenarios, it has been used both for heat and particle transport for this kind of scenarios. For the advanced regimes, CDBM transport model has been also considered for heat transport whereas GLF23 has been always used for particle transport.

The density at the separatrix and at the top of the pedestal has been fixed to experimental values. In order to do this, the GLF23 transport model has been applied from the magnetic axis up to the top of the pedestal while outside that point, the transport has been adjusted by assuming that the particle diffusivity is proportional to the ion neoclassical heat transport, i.e. $de, i = C\chi_{i,neo}$, where C is a constant adjusted, C = 1 for inductive H-modes and C = 3 for hybrids. The sources considered in these simulations are the ones obtained from NBI, however, for the inductive H-mode discharges, extra recycling particle source has been adjusted at the edge in order to match the density at the top of the pedestal. The sensitivity of the results to the NBI sources will be analyzed.

In figure 12 and 13, the CRONOS simulation of the JET discharge 73344 and JT-60U discharge 33654 are shown. The density profile is reasonably well simulated, whereas the temperatures do not differ from the ones obtained from the fixed density simulations. In particular, the low density peaking characteristic of the inductive regimes is recovered by this model, although the density profile for the discharge JT-60U 33654 is slightly overestimated.

The hybrid shots, 75225 from JET and 48158 from JT-60U have been simulated with both GLF23 or CDBM for heat transport and GLF23 for particle transport. The higher peaking obtained in these scenarios is generally well reproduced by the simulations, as shown in figure 14 and 15. In the case of 75225, the simulation with GLF23 slightly overestimates the peaking, in agreement with previous analyses [23], whereas simulation with GLF23 and CDBM slightly underestimates it. Regarding the temperatures, they are close to the ones obtained with fixed density profile. In the case of the JT-60U shot 48158, the trend is the opposite, which can be explained by the overestimated ion temperature profile, whereas when the simulation is performed with GLF23 + CDBM the density tends to be closer to experimental data. In any case, both simulations cover the experimental data and give a margin of confidence for future extrapolations.

The fact that the simulations are able to reproduce the transition from low density peaking for inductive H-modes to high density peaking for hybrid scenarios is of particular interest for the extrapolation to JT-60SA, a device particularly focused on advanced scenarios. The density

peaking generates more bootstrap current, something essential for the self-sustainment of advanced regimes in future devices as JT-60SA and ITER [24]. In order to analyse the reasons for the extra peaking in advanced regimes, two alternative simulations have been done for both JET discharge 75225 and JT-60U 48158 by removing the particle source from the NBI and setting $\alpha_{ExB} = 0$ in the simulations with GLF23. In figure 16, results show as both ExB flow shear and particle source have a similar impact on the density peaking, which is reduced from $n_e (\rho = 0.2)/< n_e > = 1.67$ to $n_e (\rho = 0.2)/< n_e > = 1.27$ for the JET shot 75225 and $n_e (\rho = 0.2)/< n_e > = 1.91$ to $n_e (\rho = 0.2)/< n_e > = 1.62$ for the JT-60U shot 48158 when both effects are not taken into account simultaneously. However, the strong effect of the ExB flow shear on the density has to be carefully analyzed since, as previously shown, this effect is overestimated by this transport model. The impact on JT-60SA scenarios will be analyzed in the following sections.

From the discharges selected in this study, self-consistent simulations of particle transport, heat transport and pedestal temperature have been performed for the discharges 33654 and 48158 from JT-60U and 73344 and 75225 from JET. In order to calculate the pedestal temperature, the following scaling from [7] is used

$$W_{ped} = 0.000643 I^{1.58} R^{1.08} P^{0.42} n^{-0.08} B^{0.06} \kappa_a^{1.81} \varepsilon^{-2.13} m^{0.2} F_q^{2.09} \tag{2}$$

where I is the current (MA), R major radius (m), P thermal loss power (MW), n density (10^{-19} m^{-3}), B toroidal field (T), κ_a elongation, ε aspect ratio, m atomic mass and F_q ($\equiv q_{95}/q_{cyl}$ with q_{cyl} defined as $5\kappa_a^2 B/RI$ with a minor radius). The position of the top of pedestal is fixed to the experimental value.

In figures 17 and 18 the electron density and temperature profiles obtained by CRONOS are compared with experimental data for the JT-60U discharge 33654 and JET discharge 73344. The temperature at the top of the pedestal is slightly overestimated for JET discharge 73344, which leads to a pressure of 20kPa, higher than the experimental one, 15kPa. For the JT-60U discharge 33654, the predicted pressure, 13kPa, is closer to the experimental one. The profiles obtained from these simulations are similar to the ones obtained with fixed pedestal pressure; however, due to the stiff behaviour of the GLF23 transport model, the overestimation or underestimation of the pedestal leads to differences on average temperatures that follow the same trend, as shown in table II.

Simulations for the JET discharge 75225 and JT-60U 48158 are shown in figure 19 and 20. The pedestal pressure slightly depends on the model applied for simulating the core turbulence. The reason is the slightly different densities at the top of the pedestal which, from expression 2, has an impact on the pedestal stored energy, higher for lower densities. The change on the plasma equilibrium also has an impact on the q profile, a factor that also plays a role in expression 2. In particular, when using GLF23 for temperatures and density, the pedestal pressure obtained for the JET discharge 75225, 8.2kPa is below the experimental one 10kPa. However, when the model CDBM is applied for the temperatures the pedestal is matched. This different pedestal pressure does not lead to the same trend on the core profiles because of the different stiff behaviour of the

6

models, as shown in figure 19. In spite of the fact that the ion temperature pedestal is higher for the CDBM model, the core ion temperature is lower, due to the limited stiffness of this model.

The pedestal pressure for the JT-60U discharge 48158 is better predicted, 5kPa for the simulation with GLF23 and 5.4kPa with CDBM, compared to 6kPa from the experiment. The profiles obtained by means of these predictions are similar to the ones obtained from fixed pedestal simulations.

In order to quantify the global accuracy of the set of different simulations and models applied, a statistical analysis has been carried out. For this purpose the standard expression for the root-mean-square (rms) deviation

$$rms = \left[\frac{1}{N} \sum_{i=1}^{N} \frac{\{X_{exp,i} - X_{sim,i}\}^2}{X_{exp,i}^2} \right]^{1/2} \tag{3}$$

has been used, where $X_{exp,i}$ is the value obtained from experimental profiles and $X_{sim,i}$ the simulated one for each of the predictions performed in this section, whereas N is the total number of simulations. The global variables selected for the comparison and the rms obtained for each one are shown in table II.

The calculation shows that the results are reasonably close to the experimental data. The maximum rms obtained is below 20% and it corresponds to the pedestal pressure, 18.2%. Interestingly, the rms obtained for the other variables, which depend on core profiles but also on the pedestal features, are lower. One reason is the counteracting effects between core models and edge models. One clear example is the simulation of the ion temperature of the discharge 75225 by means of the transport model GLF23. As shown in section 2, this model overestimated the ion temperature when including experimental rotation, however, as the pedestal is underestimated for this discharge, the average ion temperature, $< T_i > = 3.1$keV is quite close to the experimental one, $< T_i > = 3.2$keV.

5. FULLY PREDICTIVE SIMULATIONS FOR JT-60SA

Predictions for different JT-60SA scenarios have been carried out with CRONOS following the general results presented in the previous sections. Here only the flat-top stationary regime is simulated, whereas the analysis of the full scenario has been already carried out with simplified models in [1]. For this purpose, simulations including plasma current, heat and particle transport as well as pedestal have been performed. The general boundary conditions, in terms of magnetic and geometric quantities as well as the amount of heating power, have been obtained from previous 0-D simulations [1] and no further optimization or analysis has been carried out. In the case of inductive H-mode, the transport model GLF23 has been used for simulating both density and temperatures. In the case of hybrid scenario, GLF23 has been used for particle transport, and two simulations, one with GLF23 and another one with CDBM have been considered for heat transport. Since the impact of rotation is overestimated when using GLF23, no source of torque has been taken into account, i.e. no rotation is considered.

The density at the top of the pedestal has been simulated by reducing anomalous transport to ion heat neoclassical transport in the same way as done in section 4, $d_{e,i} = C\chi_{i,neo}$. The constant $C = 2$ has been chosen as an average of the ones used in section 4 for simulating the density profile in the different scenarios. No edge particle source has been considered in these simulations and the sensitivity of the scenarios to the different possible average densities has been taken into account for the standard inductive H-mode by performing an alternative simulation with $C = 1$ and keeping the density at the edge constant at $1.0 \times 10^{19}\text{m}^{-3}$. For the hybrid scenario, since two models are already used, leading two different density profiles, no further sensitivity analysis has been performed. An analysis of the interplay between particle source from edge neutrals and the scenarios analysed here will be performed in the future. The temperature at the top of the pedestal is calculated by using the expression (2) whereas the width has been adjusted to follow the scaling $\Delta\psi_N = 0.076\beta_{p,ped}^{1/2}$ [25], where ψ_N is the normalized poloidal flux and $\beta_{p,ped}^{1/2}$ is the poloidal beta, $\beta_p = 2\mu_0 <P>/\beta_p^2$, with β_p the poloidal magnetic field, calculated at the top of the pedestal.

The heating sources are simulated by using NEMO/SPOT (including for particle source) for the NBI and REMA [26] for the Electron Cyclotron Resonant Heating and Current Drive (ECRH/ECCD). The possible sawteeth are simulated by including a continuous sawteeth model which takes into account the increase of heat and particle diffusivities when $q < 1$.

The general results obtained for the inductive H-mode and the hybrid scenarios are shown in table III. The Greenwald fraction for the inductive scenario is $f_{Gr} = 0.50$ and an alternative scenario with higher density, which leads to $f_{Gr} = 0.75$, is also considered. In figure 21, the density, temperature and pressure profiles are shown for this scenario. The two densities at the top of the pedestal are $n_{e,ped} = 5.0 \times 10^{19}\text{m}^{-3}$ and $n_{e,ped} = 6.5 \times 10^{19}\text{m}^{-3}$ which are in the range of the inductive discharges from JET 73344 and 77070 analysed in section 2. A wide region of sawteeth, $0 < \rho < 0.45$ is found, which flattens the density and temperature profiles in that region. The temperatures at the top of the pedestal are $T_{ped} = 3.8\text{keV}$ for the low density and $T_{ped} = 2.4\text{keV}$ for the high density. The pressure at the top of the pedestal is higher for the low density case, $P_{ped} \sim 55\text{kPa}$ compared to the high density one, $P_{ped} \sim 45\text{kPa}$. This feature leads to an overall better performance for the lower density case with a total stored thermal energy $W_{th} = 23.2\text{MJ}$ and $\beta_N \sim 3.2$, with respect to the high density case: $W_{th} = 21.5\text{MJ}$ and $\beta \sim 2.8$. The width of the pedestal, calculated with the expression $\Delta\psi_N = 0.076\beta_{p,ped}^{1/2}$, is found to be $\rho \approx 0.94$ in both simulations.

The density, temperatures and total pressure profiles for the hybrid scenarios obtained both with GLF23 and with CDBM are shown in figure 22. The average density is higher when the CDBM transport model is used for simulating the temperatures profiles as the density at the top of the pedestal is $n_{e,ped} = 3.8 \times 10^{19}\text{m}^{-3}$ compared to $n_{e,ped} = 3.4 \times 10^{19}\text{m}^{-3}$ when only GLF23 is used. These values are close to hybrid regimes obtained on JET. The pedestal width is slightly narrower than in the inductive scenario, $\rho \approx 0.95$, in both simulations. The temperature profiles for both simulations are slightly different, with lower temperature at the edge and higher temperature peaking in the core for the simulation with CDBM. However, in both cases, the average temperatures are

similar. The pedestal pressure is also similar in both cases, $P_{ped,GLF23} = 28kPa$, $P_{ped,CDBM} = 32kPa$, and therefore the energy thermal confinement is similar $H_{98}(y,2) = 1.15$ for the simulation with GLF23 and $H_{98}(y,2) = 1.25$ for the CDBM one. In the case of the q profile, the sawteeth radius is much reduced in comparison with the inductive scenario, as shown in figure 23.

CONCLUSIONS

An optimum set of models for the JT-60SA 1.5D scenario modelling has been obtained by analyzing core turbulence and pedestal MHD characteristics of selected discharges from JT- 60U and JET, which share characteristics with JT-60SA.

For inductive H-modes, for which ITG modes are found to be dominant in the core, heat and particle transport can be reasonably well simulated using the GLF23 transport model. The temperatures obtained are close to experimental data and the low density peaking, characteristic of these regimes is also recovered.

However, for hybrid scenarios, the agreement between models and experimental data is less reliable. GLF23 tends to overestimate turbulence reduction by ExB shear leading to too high ion temperature profiles. Moreover, for plasma discharges, like the JT-60U 48158, in which TEM are dominant, it also overestimates the turbulence transport driven by these modes. Therefore, the application of this transport model for those plasma conditions is doubtful. On the other hand, the CDBM transport model tends to give temperatures closer to experimental data in this regime, provided that the model is amended in order to take into account the high fast ion population typical of this scenario, which provides a significant reduction of turbulence. Regarding particle transport, GLF23 is able to reproduce the increase of density peaking usually obtained in these regimes.

The pedestal temperatures have been simulated by using the scaling shown in expression (2) and obtained from ref 7. Simulations including this scaling together with particle and heat transport have been performed for JT-60U and JET inductive and hybrid discharges. The general rms is below 20% for the average densities and temperatures as well as for the pedestal pressure.

The analysis previously carried out gives a framework for JT-60SA modelling which has been used to simulate two scenarios: inductive H-mode and hybrid. In general, the typical characteristics of each scenario have been recovered with the present design of machine subsystems on JT-60SA. In particular, a large sawteeth radius, $\rho \sim 0.45$, with $q_{95} \sim 3$, moderate density peaking and thermal improved confinement $H_{98}(y,2) \sim 1$ has been found for inductive H-mode at $Ip = 5.5MA$ when 41MW of input power is added. The pedestal pressure is $Pped \sim 50kPa$ located at of $\rho = 0.94$. For the hybrid scenario, at lower total current, $Ip = 3.5MA$, and input power, 37MW, $q_{95} \sim 4.5$ with $q < 1$ only for $\rho < 0.2$ and $H_{98}(y,2) \sim 1.2$ is obtained. The pedestal pressure is $Pped \sim 30kPa$ located at $\rho = 0.95$. This confirms, on the basis of the analysis of present day experiments, that the power and magnetic systems available on JT-60SA are adequate for the operation of these plasma scenarios defined in [1]. However, free boundary simulations are needed in order to fully confirm this point. The simulation framework here analyzed is a good starting point for deeper analyses involving

more sophisticated models for heat and particle transport, as TGLF [21], which has been shown to properly account for heat fluxes in advances scenarios [27] and in particular for an extensive analysis of the impact of particle edge sources, which can modify the scenarios obtained in this paper [28], and the influence of the high population of fast ions generated by the JT-60SA NBI system on turbulence [29,30] and on the sawteeth period. Pedestal predictions for JT-60SA based on peeling ballooning mode analyses will be carried out on the basis of the scenarios here found and will be compared with the predictions obtained.

ACKNOWLEDGEMENTS

REFERENCES

[1]. JT-60SA Research Plan -Research Objectives and Strategy Version 3.0 2011, December, http://www.jt60sa.org/pdfs/JT-60SA_Res_Plan.pdf

[2]. Erba M. et al., Plasma Physics and Controlled Fusion **39** 261 (1997).

[3]. Honda M. et al., Nuclear Fusion **46** 580 (2006).

[4]. Kinsey J.E. et al., Physics of Plasmas **12** 052503(2005)

[5]. Artaud J.F. et al., Nuclear Fusion **50** 043001 (2010).

[6]. Hayashi N. et al., Physics of Plasmas **17** 056112 (2010).

[7]. Cordey J.G. Nuclear Fusion **43** 670-674 (2003).

[8]. Jenko F., Dorland W., Kotschenreuther M. and Rogers B.N., Physics of Plasmas **7**, 1904 (2000).

[9]. Hobirk J. et al., Plasma Physics and Controlled Fusion **54** 095001 (2012).

[10]. Oyama N. et al., Nuclear Fusion **49** 065026 (2009).

[11]. Huysmans G.T.A. et al. CP90 Conference on Comp. Physics, Word Scientific Publ. Co. 1991, p.371.

[12]. Belli E.A. and Candy J. Physics of Plasmas **17**, 112314 (2010)

[13]. Romanelli F., Physics of Fluids B **1**, 1018 (1989).

[14]. Romanelli F. and Briguglio S. Physics of Fluids B **2**, 754 (1990).

[15]. Staebler G. et al., «Testing the Trapped Gyro-Landau Fluid Transport Model with Data from Tokamaks and Spherical Tori» TH/P8-42, 22nd IAEA Fusion Energy Conference, Geneva, Switzerland.

[16]. Huysmans G.T.A. et al., Plasma Physics and Controlled Fusion **8** 4292 (2001).

[17]. Maget P. et al., Nuclear Fusion **53** 093011 (2013)

[18]. Schneider M. et al., Nuclear Fusion **51**, 063019 (2011).

10

[19]. Schneider M., Eriksson L.G., Basiuk V. and Imbeaux F. Plasma Physics and Controlled Fusion **47** 2087 (2005).

[20]. Tani K., et al., J. Physical Society Jpn. **50**, 1726 (1981).

[21]. Voitsekhovitch, I. et al., submitted to Nuclear Fusion.

[22]. Staebler G. et al., Physics of Plasmas **12**, 102508 (2005).

[23]. Garzotti L. et al., „Simulations of density profiles in JET hybrid discharges" P1.004, 39th EPS Conference & 16th Int. Congress on Plasma Physics, Stockholm, Sweden

[24]. Garcia J. and Giruzzi G., Physical Review Letters **104**, 205003 (2010).

[25]. Snyder P.B. et al., Nuclear Fusion **51** 103016(2011).

[26]. Krivenski G.V. et al., Nuclear Fusion **25** 127 (1985).

[27]. Baiocchi B. et al., submitted to Plasma Physics and Controlled Fusion

[28]. Cesario R. et al., Plasma Physics and Controlled Fusion **55** 045005 (2013).

[28]. Garcia J. et al., submitted to Physical Review Letters

[29]. Citrin J. et al., Physical Review Letters **111**, 155001 (2013).

Discharge	q_{95}	$\varkappa/\delta$	Bt (T)	β_N	f_{Gr}	Ip(MA)	Pin (MW)
Inductive H-mode JT-60U Pulse No: 33654	3.0	1.53/0.16	3.1	1.1	0.48	1.8	10
Inductive H-mode JT- 60U Pulse No: 33655	3.0	1.53/0.16	3.1	1.1	0.48	1.8	10
Hybrid JT-60U Pulse No: 48158	3.2	1.40/0.33	1.5	2.6	0.50	0.9	7.5
H-mode JET Pulse No: 73344	3.5	1.75/0.40	2.7	1.5	0.75	2.5	12
H-mode JET Pulse No: 77070	3.5	1.75/0.40	2.7	1.5	0.75	2.5	15
Hybrid JET Pulse No: 75225	4.0	1.64/0.24	2.0	3.0	0.45	1.7	17
Hybrid JET Pulse No: 77922	4.3	1.64/0.24	2.0	2.7	0.70	1.7	17

Table I: Main characteristics of JT-60U discharges 33654, 33655, 48158 and JET 73344, 77070,75225 and 77922 where κ/δ is the elongation/triangularity, Bt is the magnetic field in the axis, β_N is the normalized beta, f_{Gr} is the ratio between the plasma density and the Greenwald density limit, Ip is the total current and Pin the injected power.

Discharge	β_N	$H_{98}(y,2)$	f_{Gr}	$<ne>10^{19}m^{-3}$	$<Te>keV$	$<Ti>keV$	Pped(kPa)
Inductive H-mode 33654	1.1/1.3	0.65/0.85	0.42/0.48	2.3/2.4	2.0/2.7	3.2/3.4	13/15
Inductive H-mode 73344	1.7/1.5	0.97/0.85	0.80/0.75	6.75/6.65	2.0/1.8	2.2/1.9	20/15
Hybrid 75225 (GLF23)	3.0/2.95	1.3/1.25	0.65/0.56	3.4/2.9	2.8/2.7	3.1/3.2	8.2/10
Hybrid 75225 (GLF23 + CDBM)	2.6/2.95	1.15/1.25	0.57/0.56	2.8/2.9	2.2/2.7	3.2/3.2	10/10
Hybrid 48158 (GLF23)	2.0/2.6	1.05/1.07	0.35/0.50	1.40/1.55	1.8/2.0	3.4/2.5	5.0/6.0
Hybrid 48158 (GLF23 + CDBM)	2.1/2.6	0.98/1.07	0.40/0.50	1.64/1.55	1.5/2.0	2.4/2.5	5.4/6.0
rms	**15.6%**	**12.2%**	**17.1%**	**8.7%**	**17.6%**	**16.3%**	**18.2%**

Table II: Comparison between the simulations performed in this section (left at each column) and the values obtained from experimental profiles (right at each column) for a number of global quantities. The rms for each quantity, representing the deviation over the set of simulation and models applied, is shown in the last row.

Scenario	Bt (T)	Pin (MW)	Ip (MA)	q_{95}	H98(y,2)	β_N/β_p	fGr	$<ne>$ x10^{19}m^{-3}	$<Te>keV$	$<Ti>keV$	Pped (kPa)
Inductive H-mode high density	2.25	41	5.5	3.0	1.0	2.8/0.80	0.75	8.7	4.1	4.2	45
Inductive H-mode low density	2.25	41	5.5	3.1	1.1	3.2/0.85	0.50	6.2	5.6	5.9	55
Hybrid GLF23	2.25	37	3.5	4.4	1.15	3.0/1.40	0.60	4.5	4.0	4.2	28
Hybrid GLF23+CDBM	2.25	37	3.5	4.4	1.25	3.2/1.45	0.65	5.0	3.7	4.0	32

Table III: Main results obtained for JT-60SA scenarios considered in this paper.
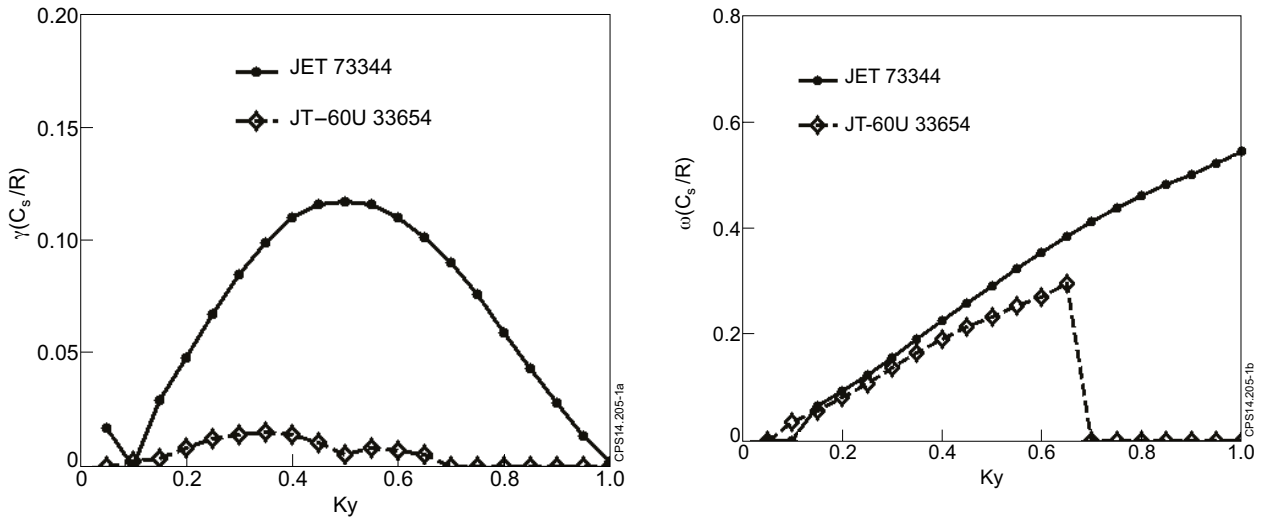
Figure 1: Linear growth rates (left) and frequencies (right) for discharges JET 73344 and JT-60U 33654.
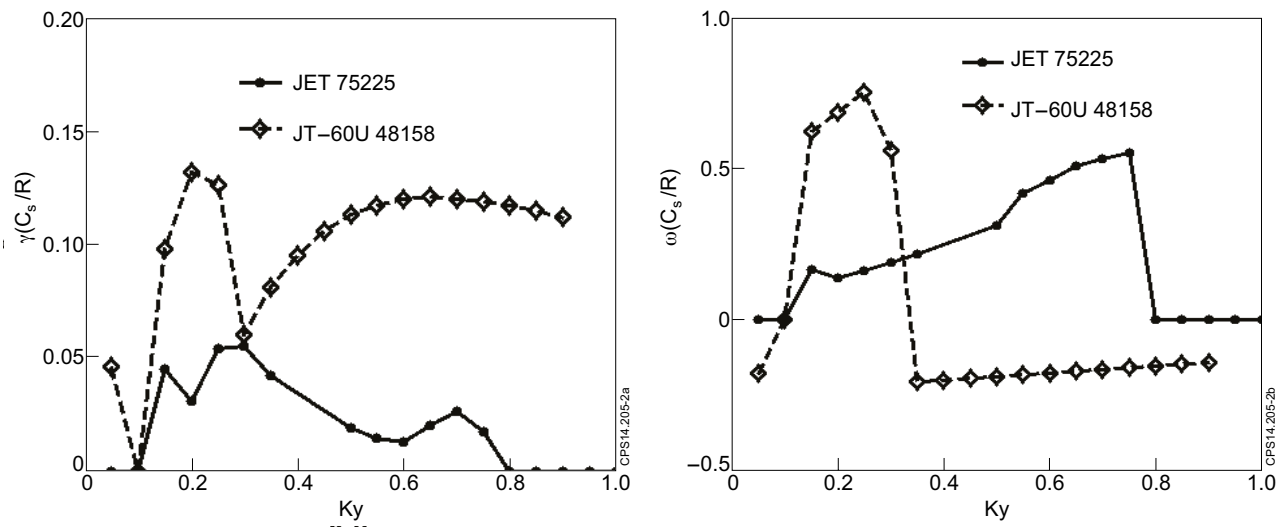
Figure 2: Linear growth rates (left) and frequencies (right) for discharges JET 75225 and JT-60U 48158.

13
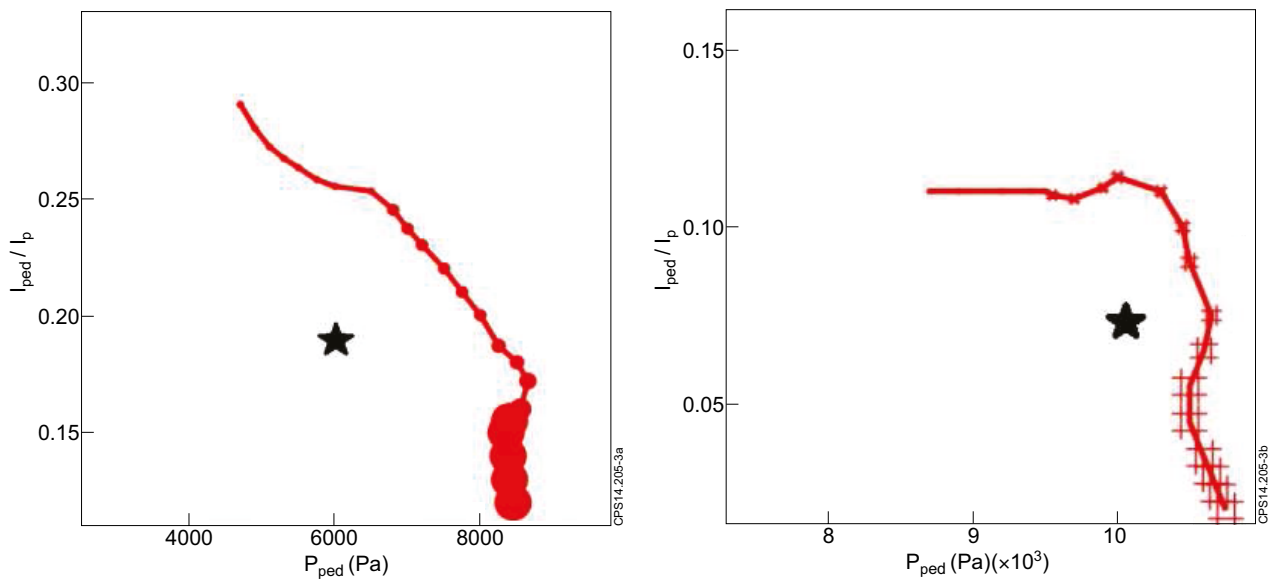
Figure 3: Peeling-Ballooning analysis of the discharges JT-60U 48158 (left) and JET 75225 (right). The experimental value is marked with a black star.

14
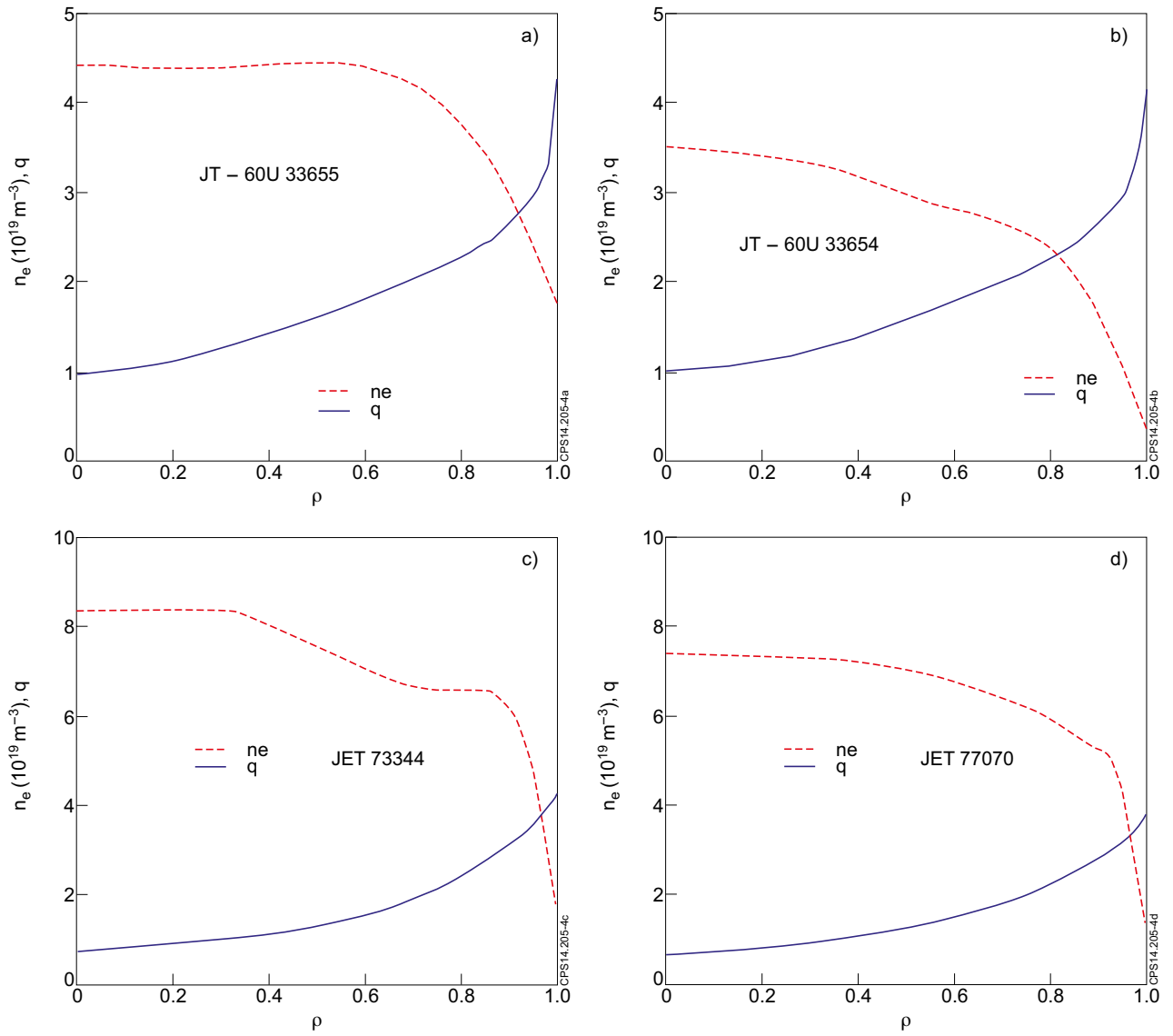
Figure 4: Fitted density and q profiles used for JT-60U discharges 33655 (a) 33654 (b) and JET discharges 73344 (c) and 77070 (d).
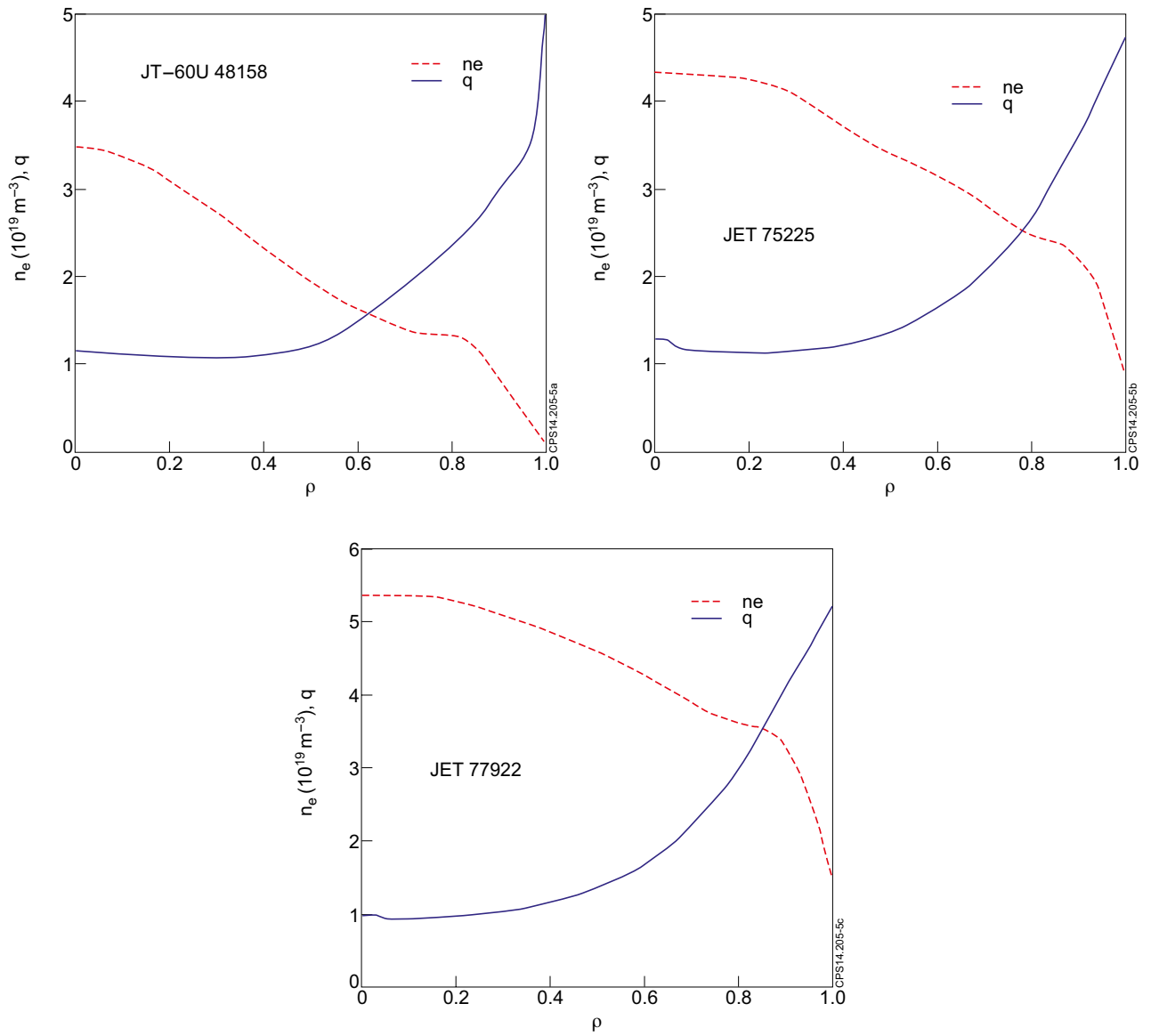
Figure 5: Fitted density and q profiles used for JT-60U discharge 48158 (left) and JET discharges 75225 (center) and 77922 (right).
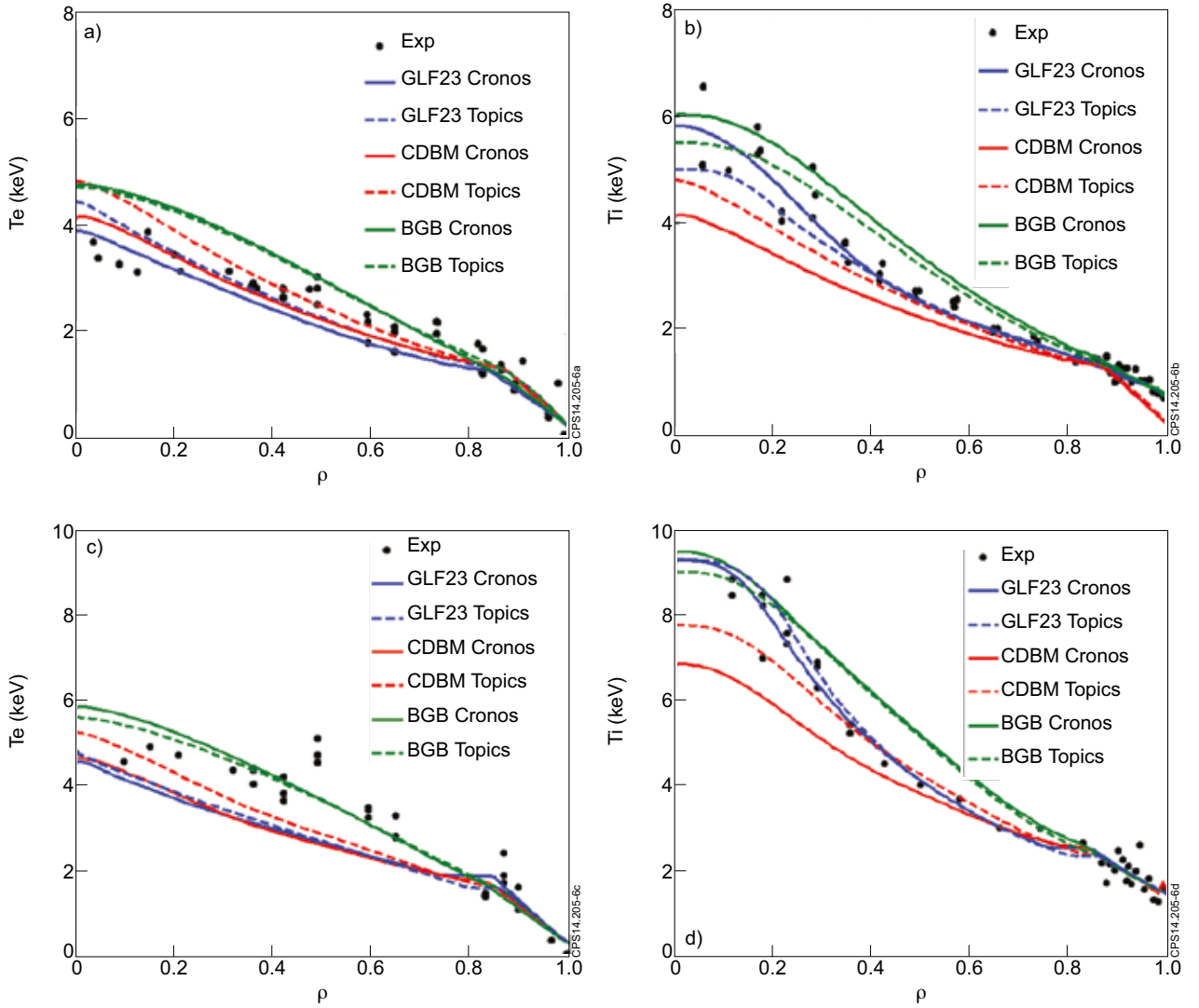
Figure 6: Comparison between the electron and ion temperatures profiles with those obtained with CRONOS and TOPICS with GLF23, CDBM and Bohm-GyroBohm transport models for the discharges 33655 (a,b) and 33654 at t = 8.0s (c,d) from JT-60U.
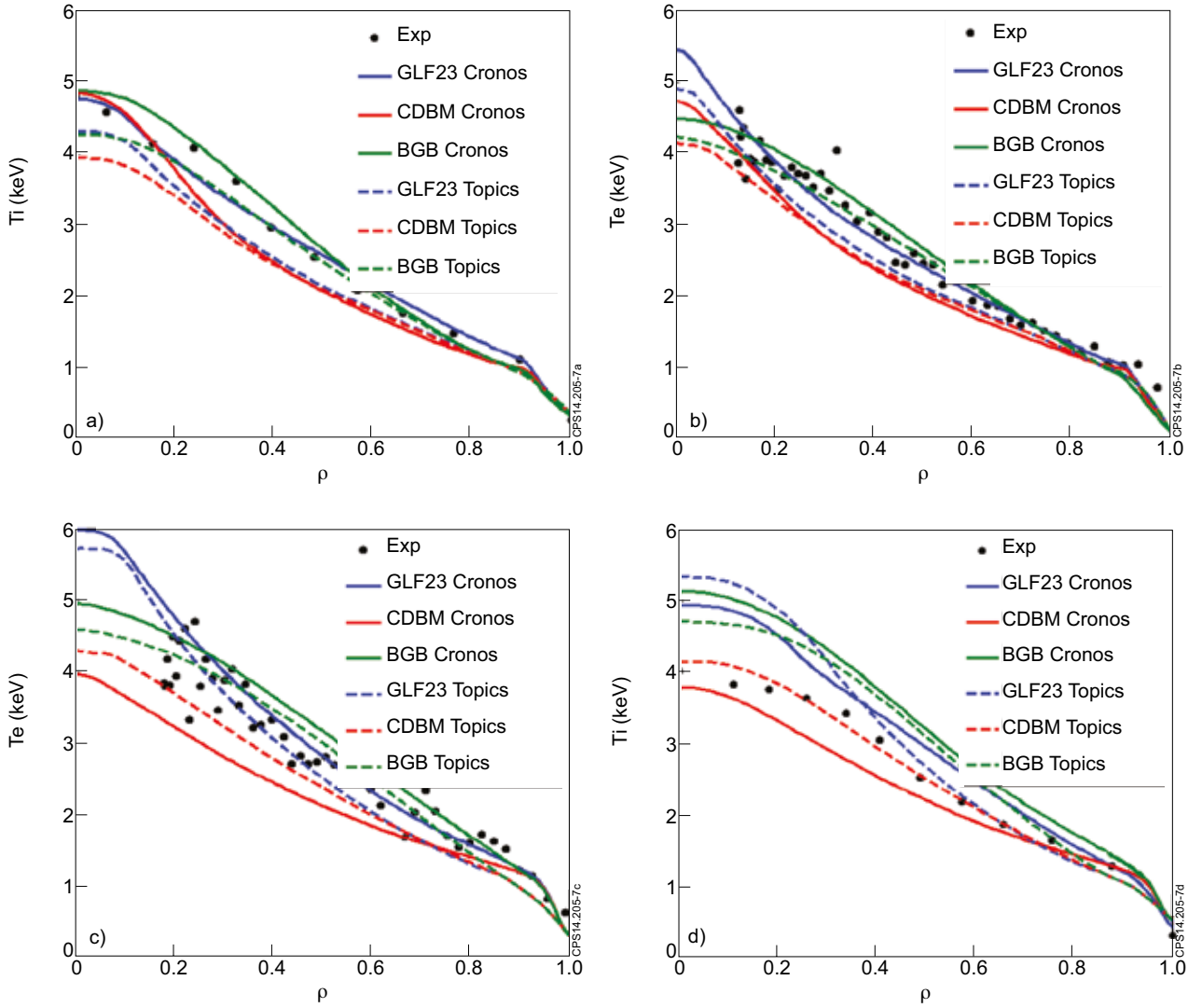
Figure 7: Comparison between the electron and ion temperatures profiles with those obtained with CRONOS and TOPICS with GLF23, CDBM and Bohm-GyroBohm transport models for the discharges 73344 at t = 19.53s (a,b) and 77070 at t = 14s (c,d) from JET.
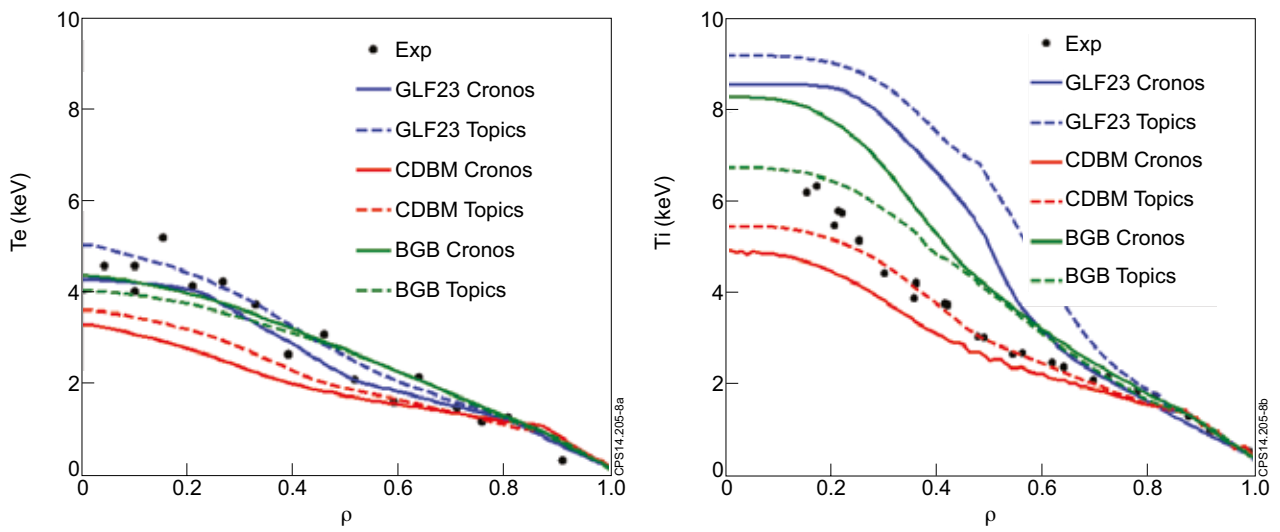
Figure 8: Comparison between the electron and ion temperatures profiles with those obtained with CRONOS and TOPICS with GLF23, CDBM and Bohm-GyroBohm transport models for the JT-60U discharge 48158 at t = 27s.
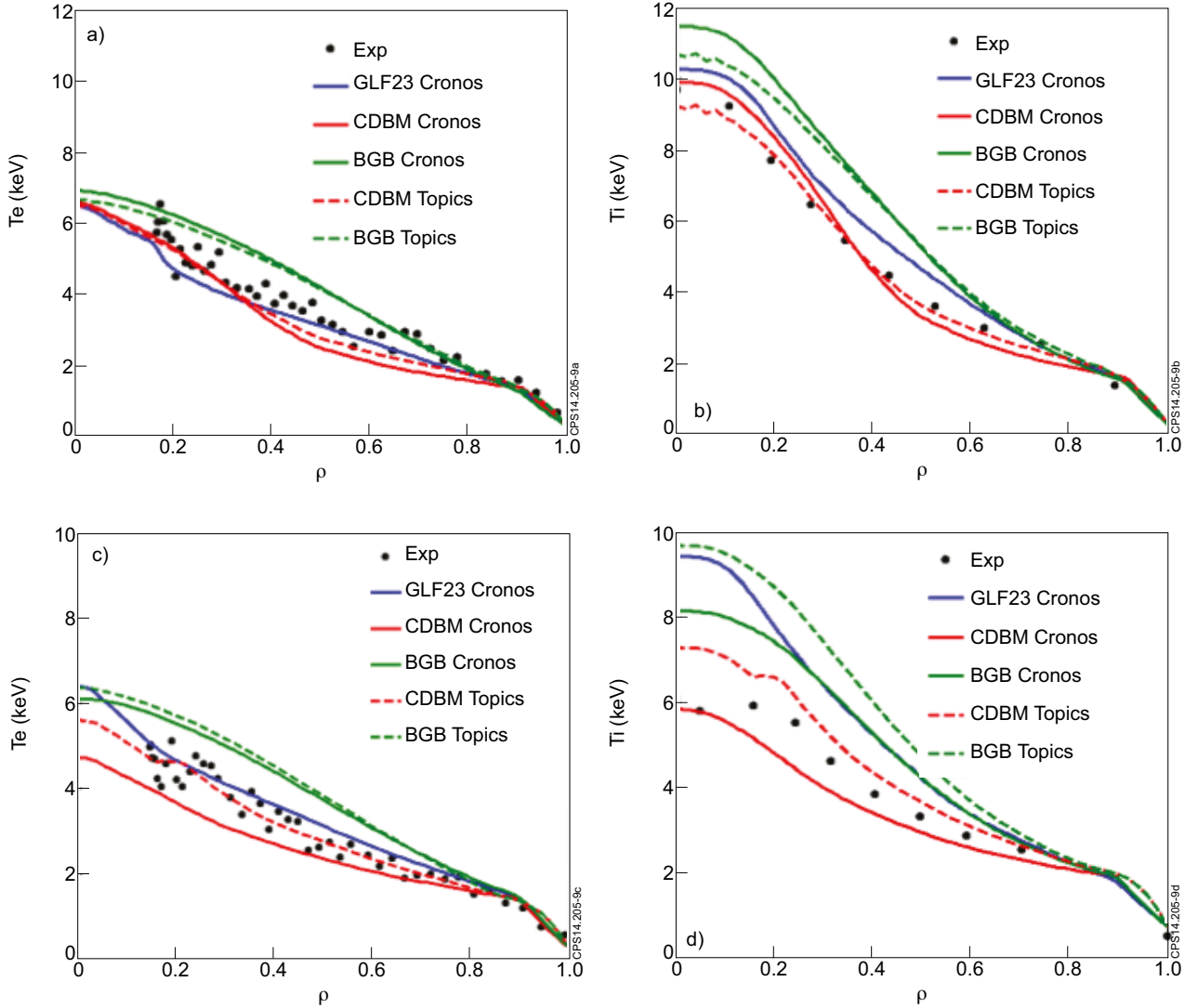
Figure 9: Comparison between the electron and ion temperatures profiles with those obtained with CRONOS and TOPICS with GLF23, CDBM and Bohm-GyroBohm transport models for the discharges 75225 at t = 6.02s (a,b) and 77922 at t = 9s (c,d) from JET.
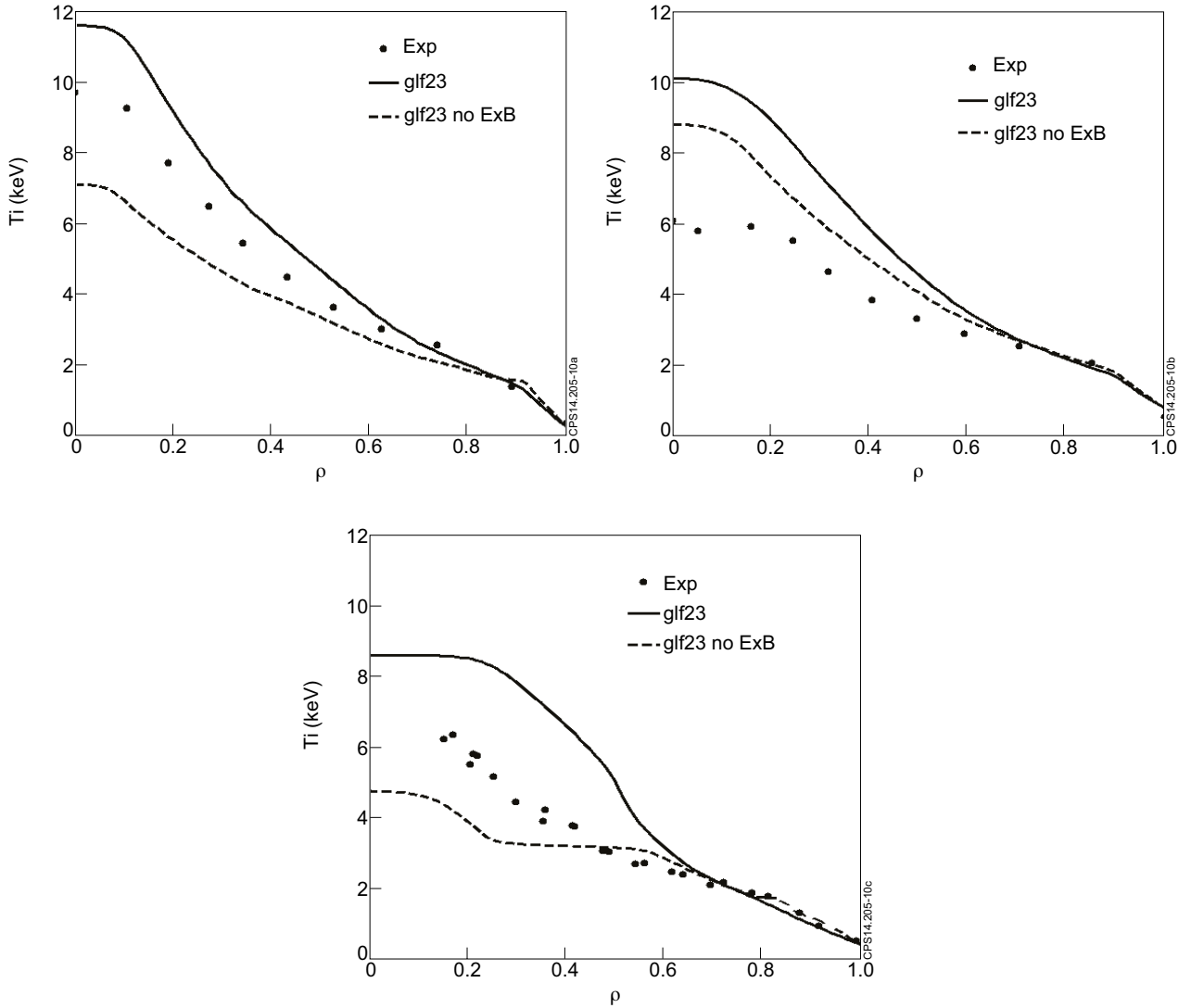
Figure 10: Comparison between the electron and ion temperatures profiles obtained with GLF23 transport model with and without the ExB shearing rate factor for the JET discharges 75225 (left) 77922 (center) and JT-60U discharge 48158 (right).
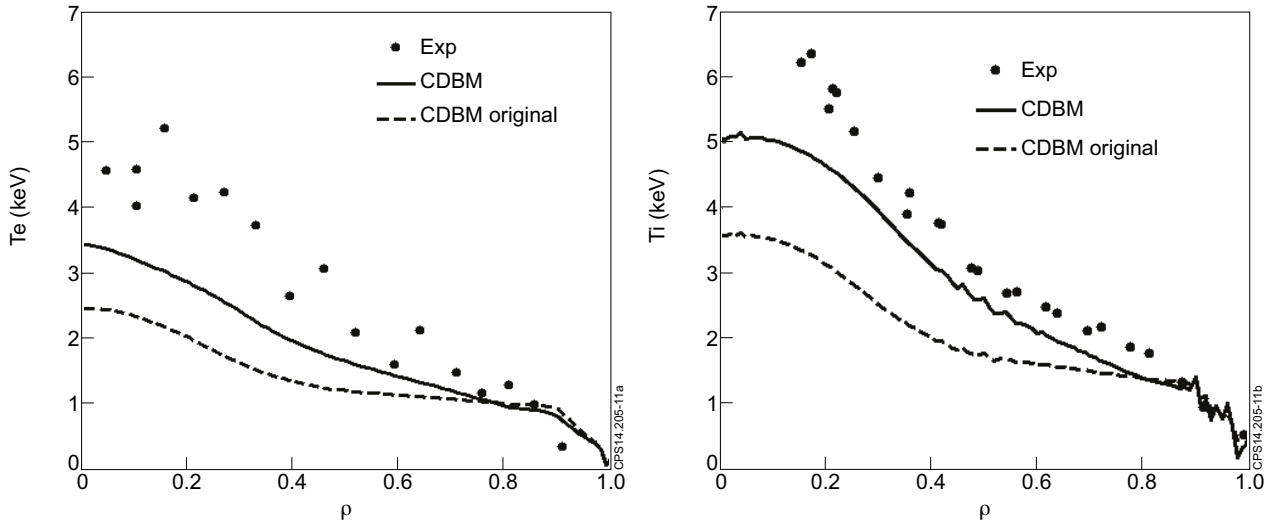
Figure 11: Comparison between the electron and ion temperatures profiles obtained with GLF23 transport model with and without the ExB shearing rate factor for the JET discharges 75225 (left) 77922 (center) and JT-60U discharge 48158 (right).
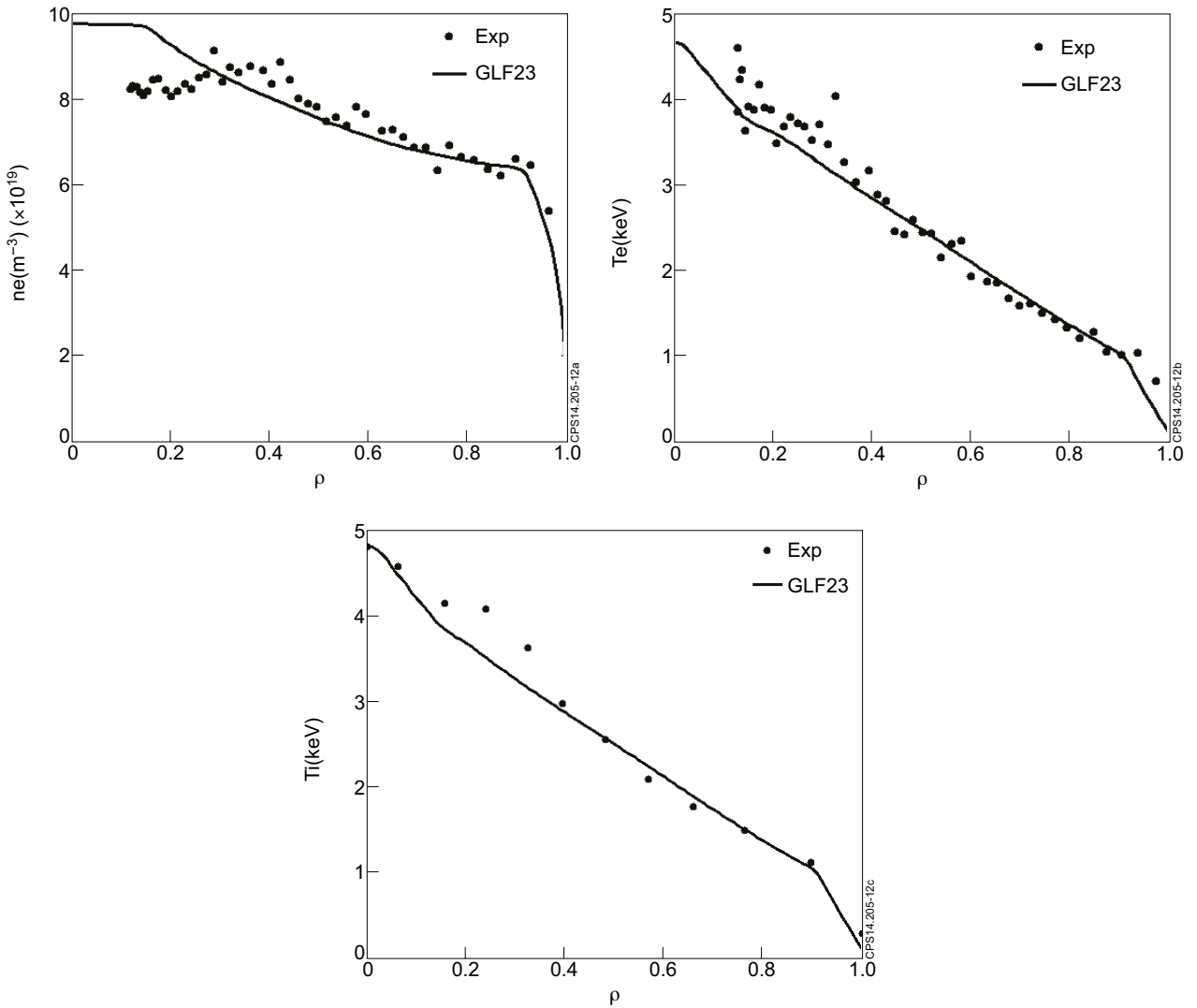
Figure 12: Comparison between the electron and ion temperature and electron density profiles with the ones obtained by using GLF23 for simulating particle and heat transport for the JET discharge 73344.
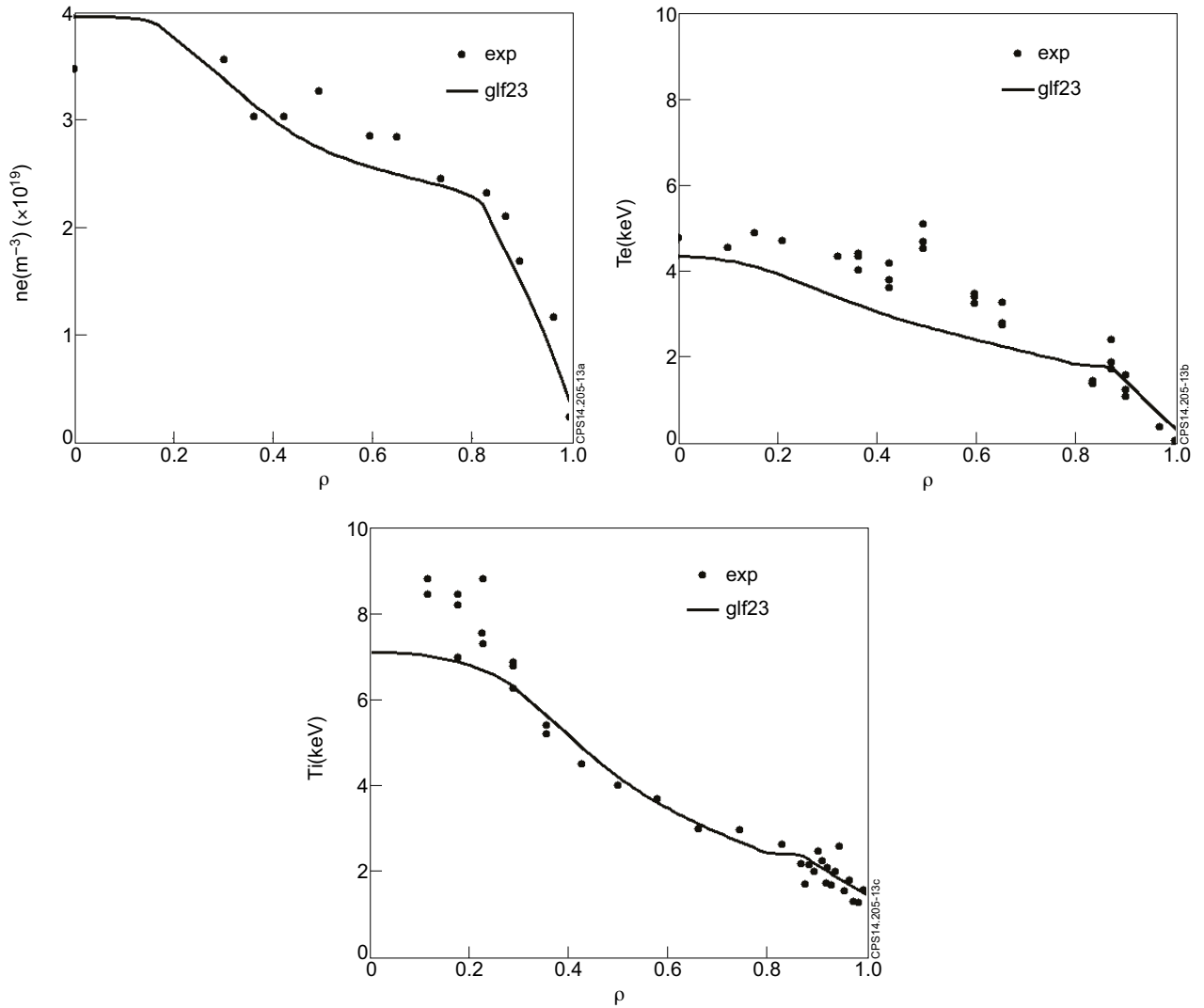
Figure 13: Comparison between the electron and ion temperature and electron density profiles with the ones obtained by using GLF23 for simulating particle and heat transport for the JT-60U discharge 33654.
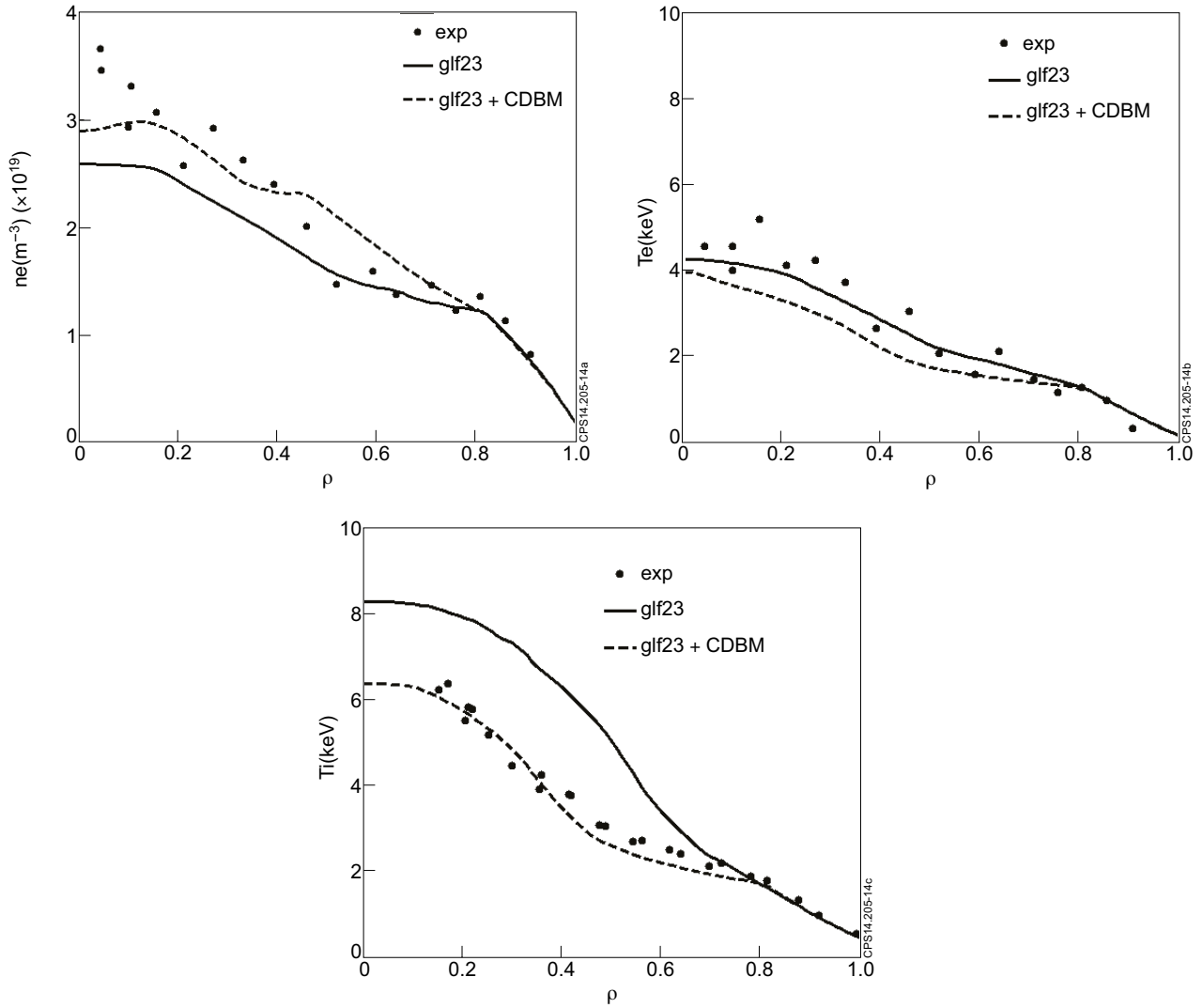
Figure 14: Comparison between the electron and ion temperature and electron density profiles with the ones obtained by using GLF23 and CDBM (only for heat transport) for simulating particle and heat transport for the JT-60U discharge 48158.
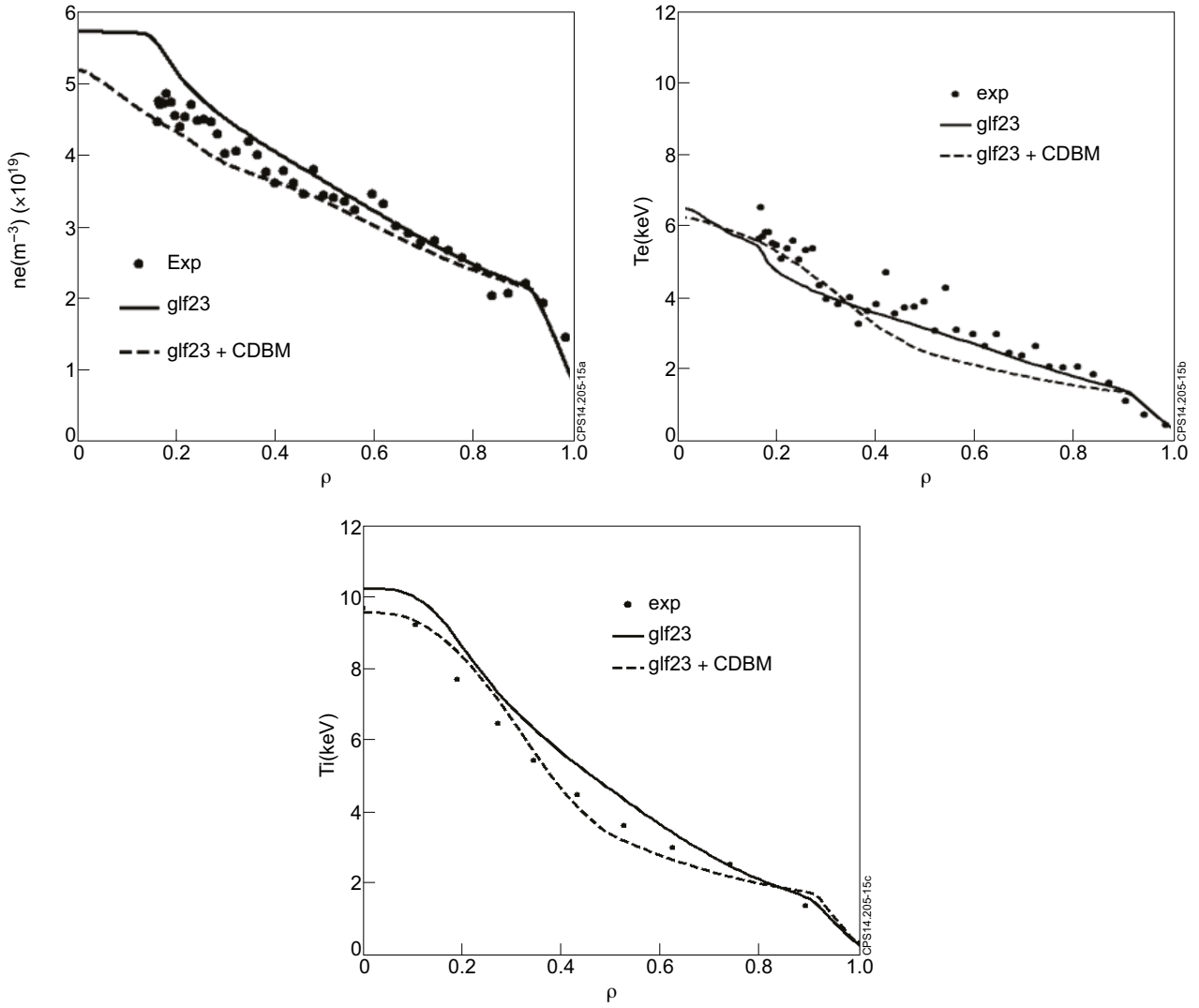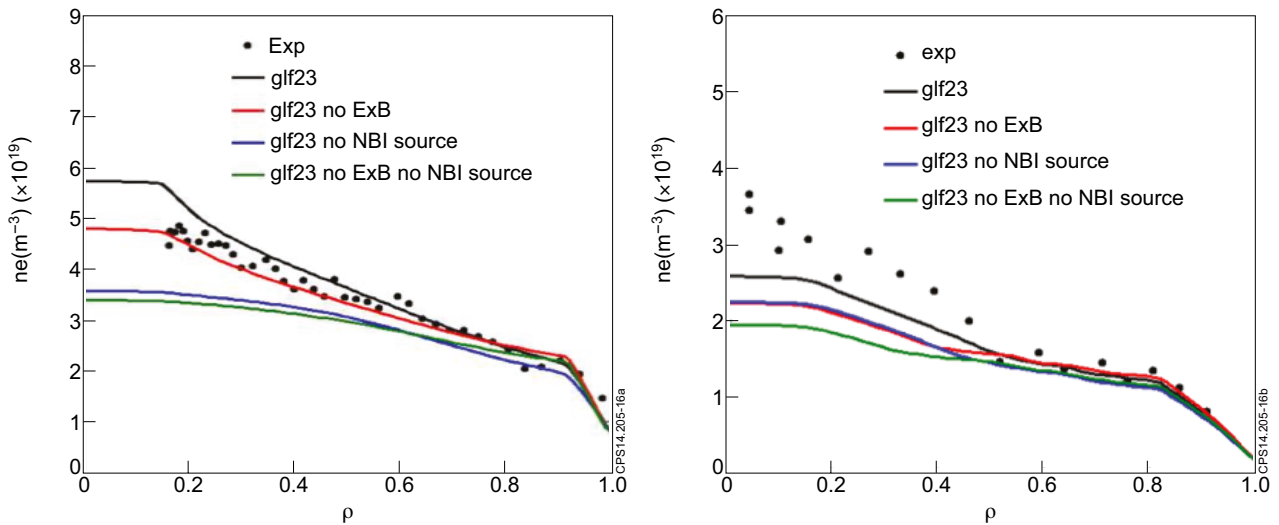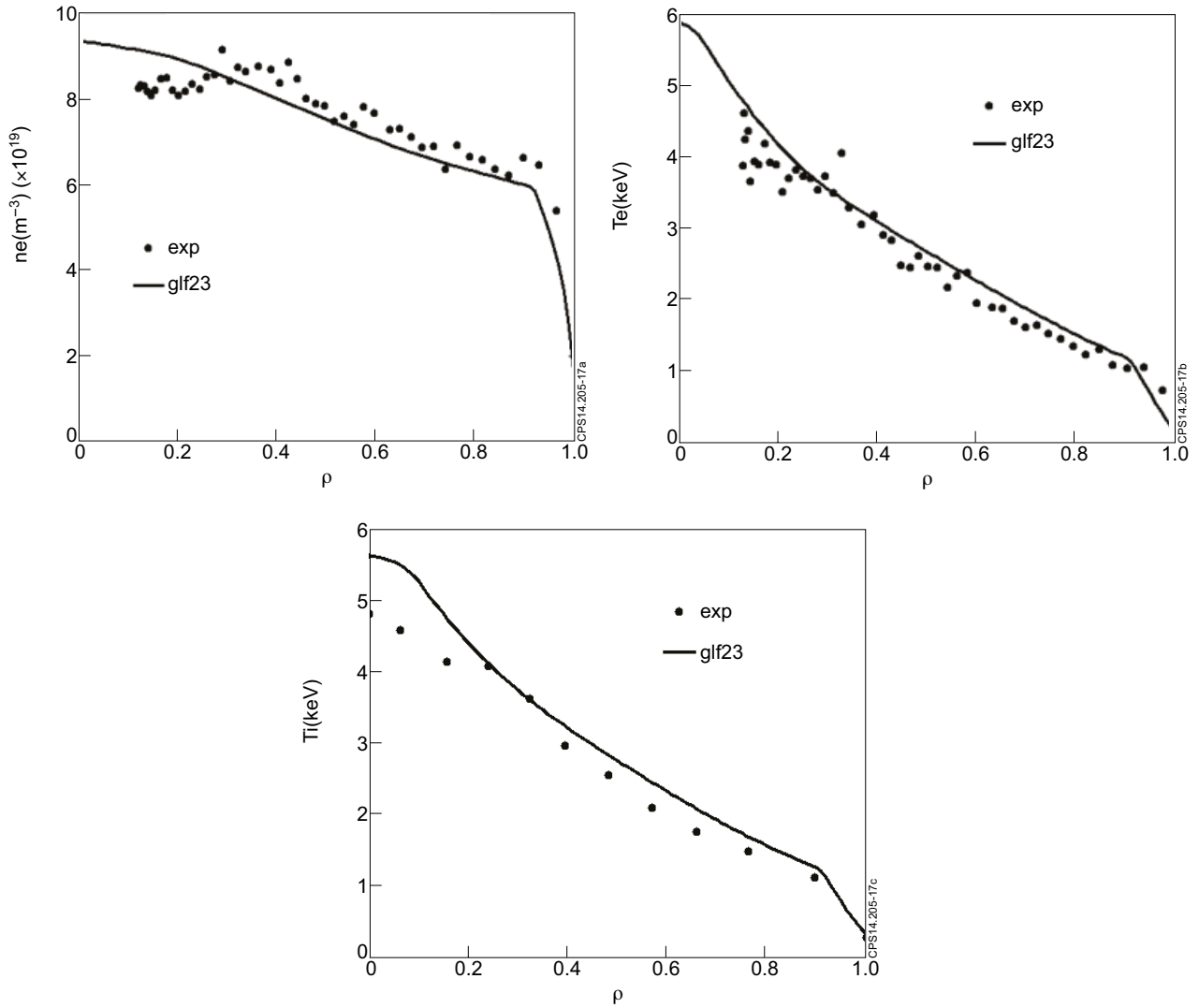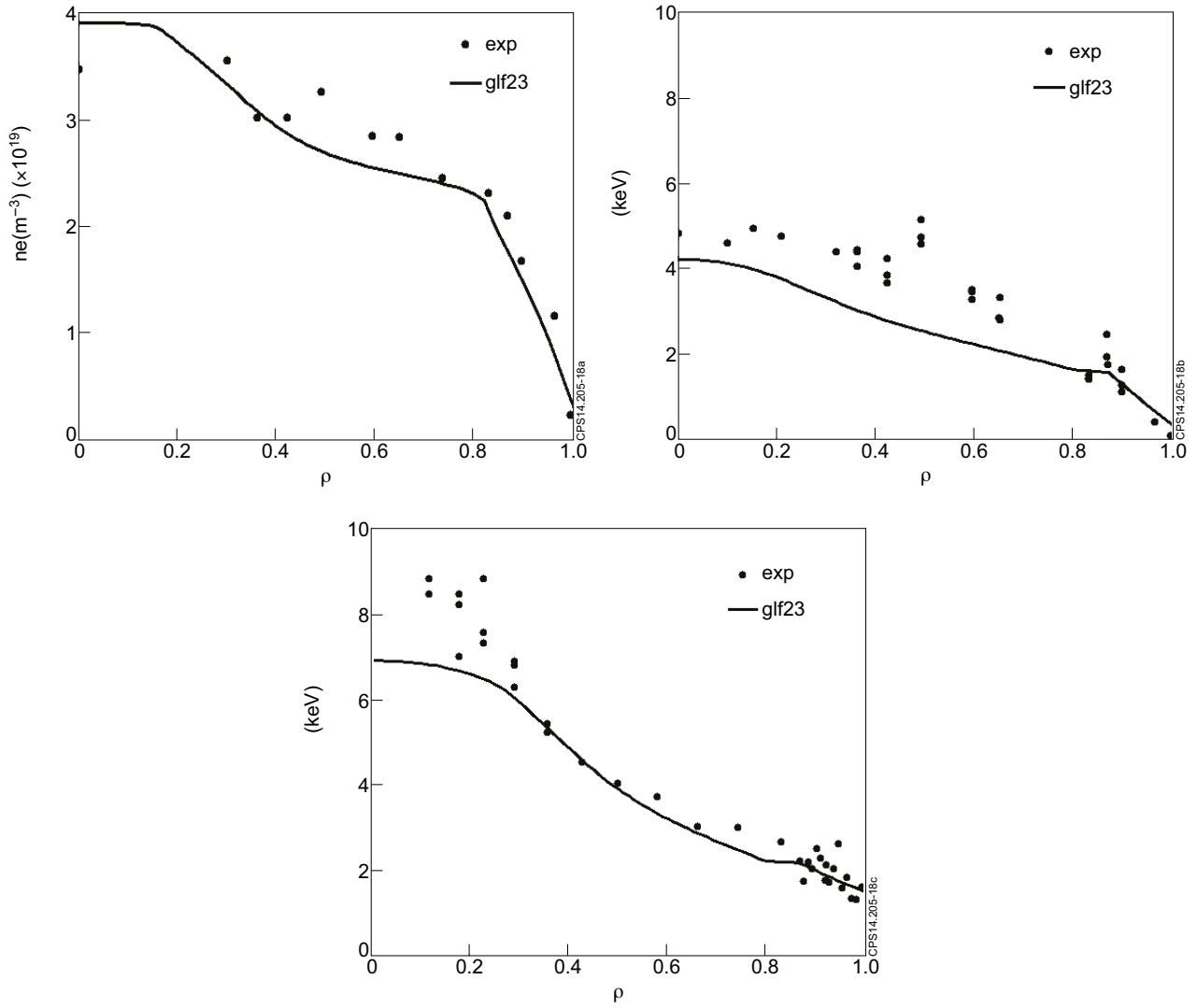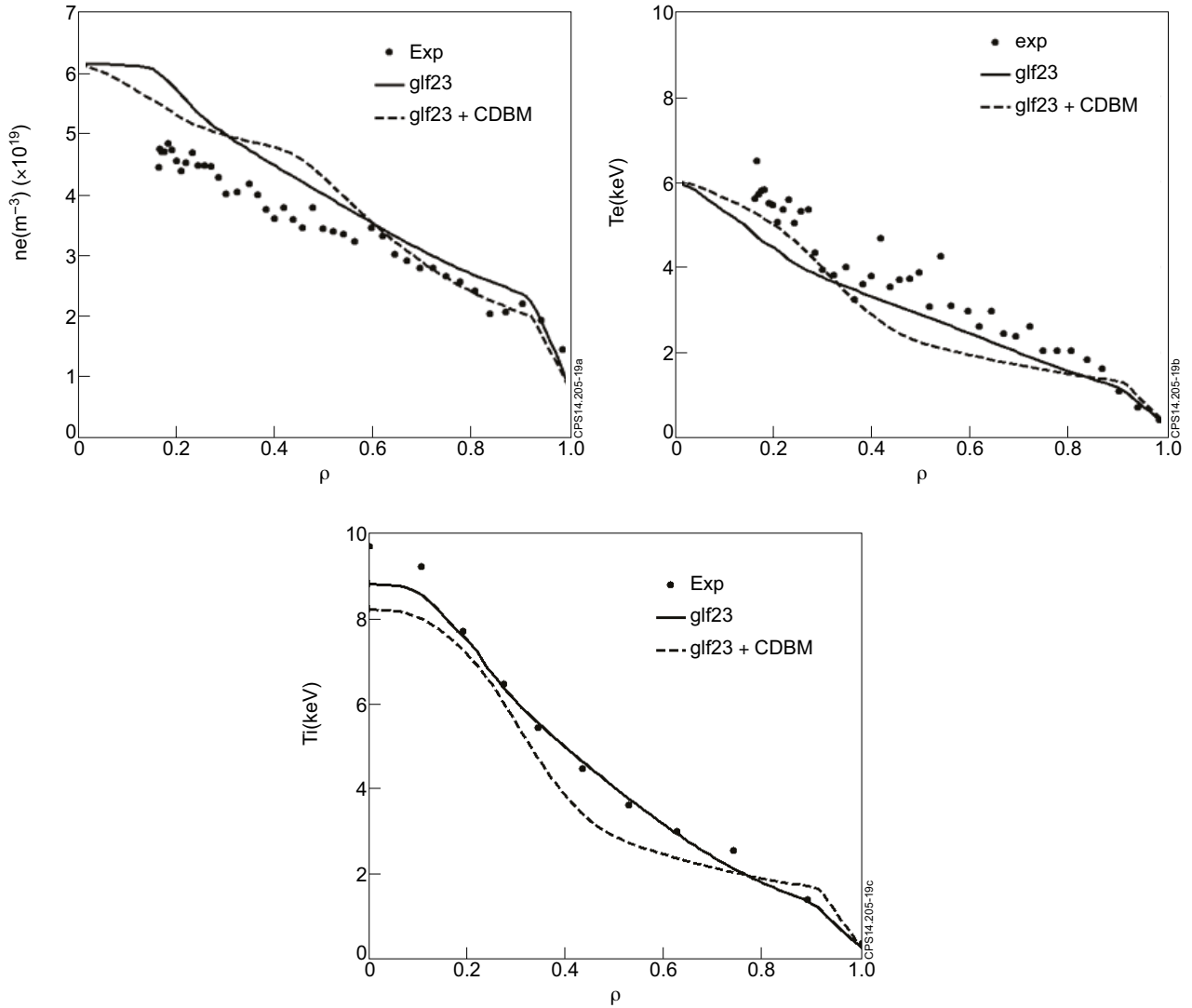
Figure 15: Comparison between the electron and ion temperature and electron density profiles with the ones obtained by using GLF23 and CDBM (only for heat transport) for simulating particle and heat transport for the JET discharge 75225.

Figure 16: Impact of ExB shearing rate and NBI particle source on density profiles for the JET discharge 75225 (left) and JT-60U discharge 48158 (right).

Figure 17: Comparison between the electron and ion temperature and electron density profiles with the ones obtained by using GLF23 for simulating particle and heat transport and scaling from (2) for the pedestal pressure for the JET discharge 73344.

26

Figure 18: Comparison between the electron and ion temperature and electron density profiles with the ones obtained by using GLF23 for simulating particle and heat transport and scaling from (2) for the pedestal pressure for the JT-60U discharge 33654.
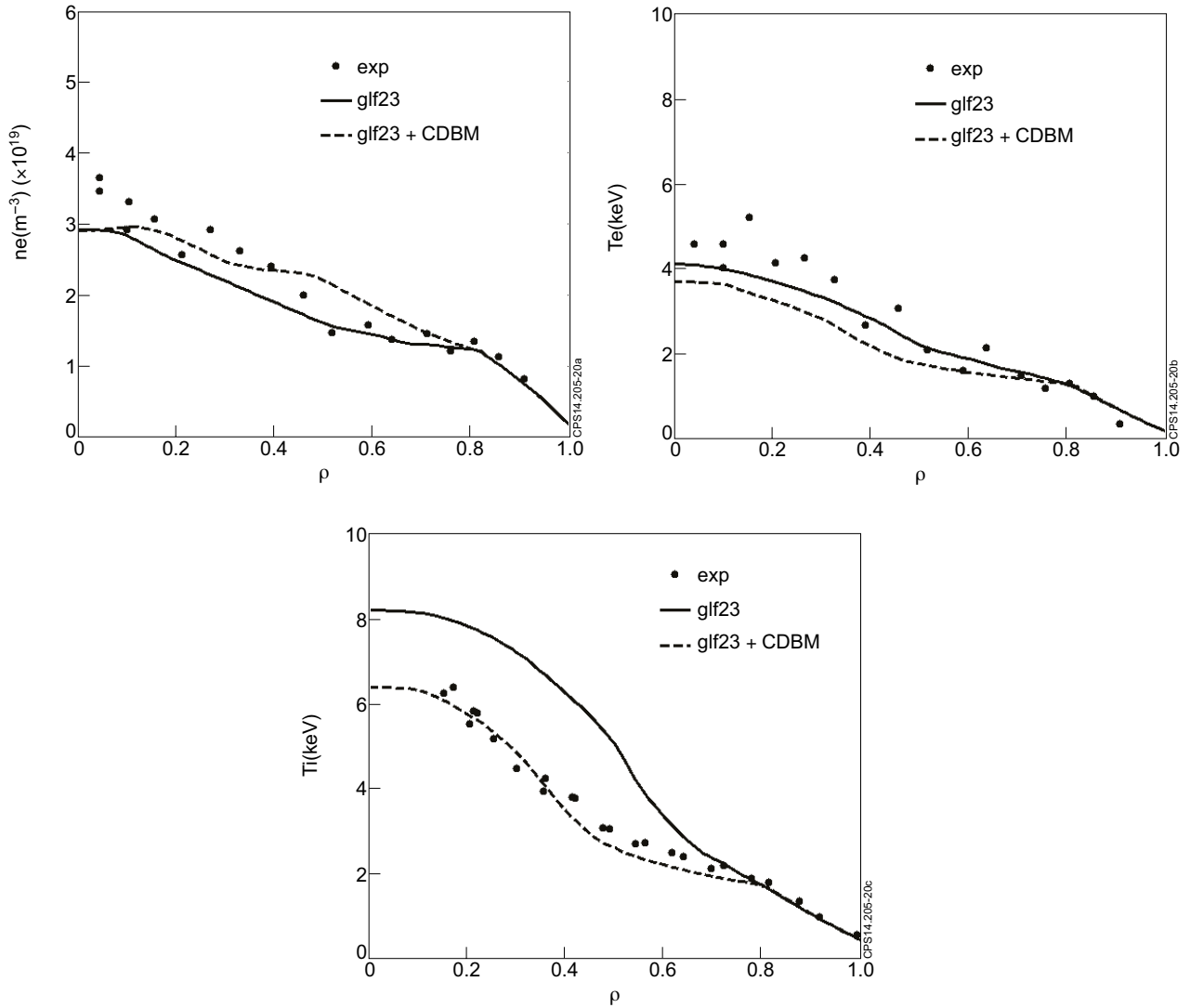
Figure 19: Comparison between the electron and ion temperature and electron density profiles with the ones obtained by using GLF23 and CDBM (only for heat transport)and scaling from (2) for the pedestal pressure for the JET discharge 75225.

Figure 20: Comparison between the electron and ion temperature and electron density profiles with the ones obtained by using GLF23 and CDBM (only for heat transport) and scaling from (2) for the pedestal pressure for simulating particle and heat transport for the JT-60U discharge 48158.
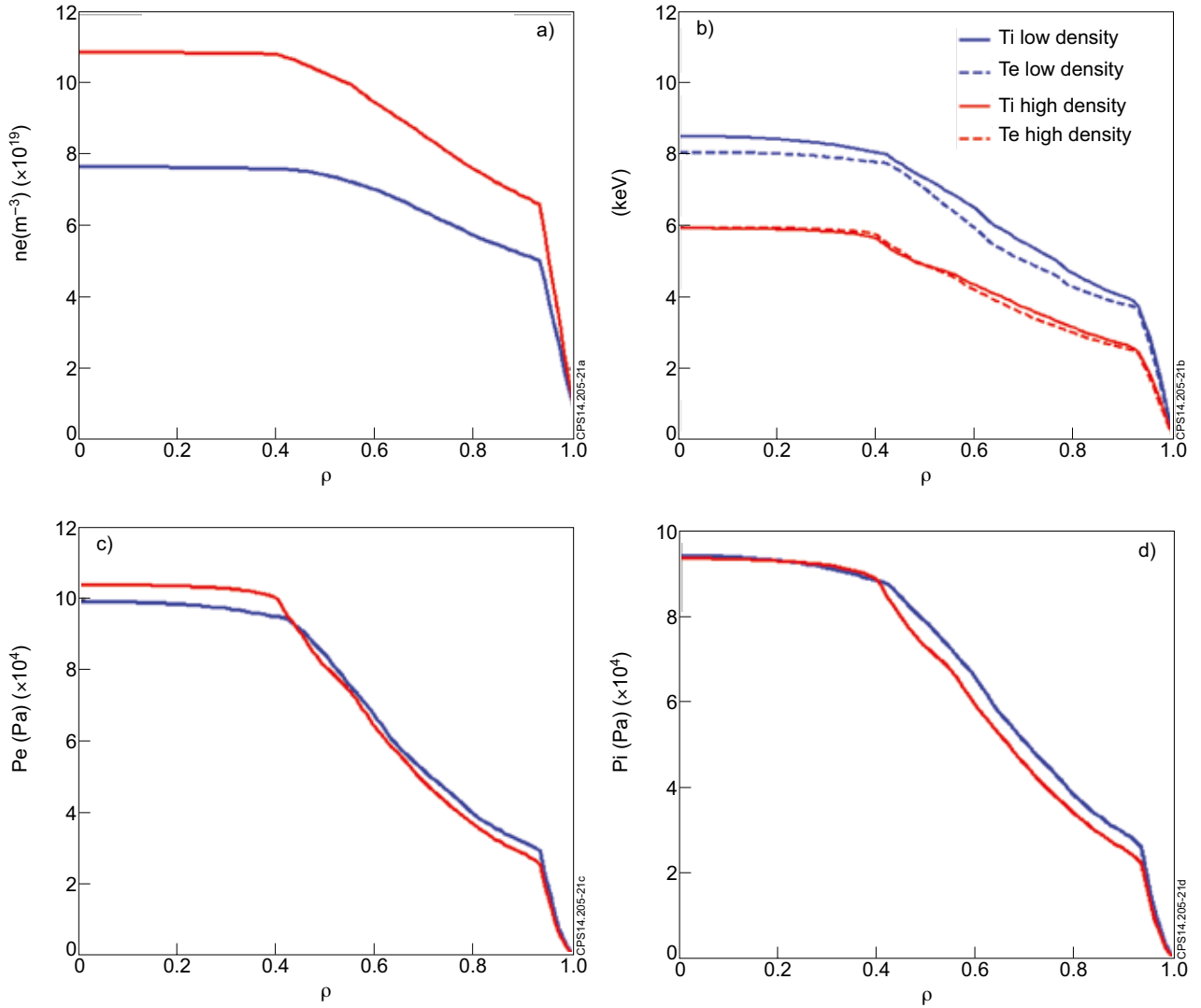
Figure 21: JT-60SA inductive H-mode simulation densities (a) Electron and ion temperatures (b) Electron pressure (c) and ion pressure (d) obtained with GLF23 transport model.
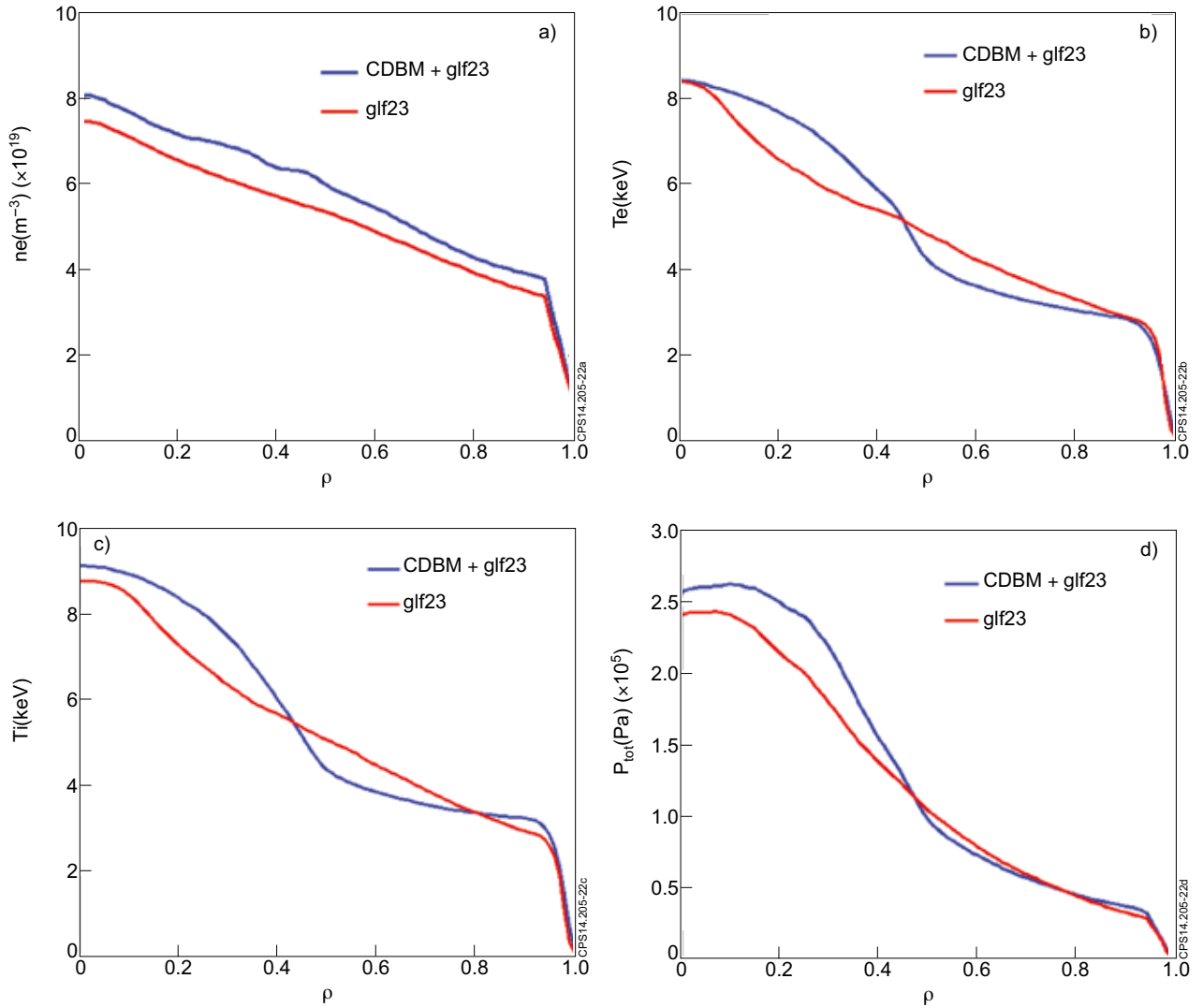
Figure 22: JT-60SA hybrid simulation densities (a) Electron temperature (b) Ion temperature (c) and total pressure (d) obtained with GLF23and CDBM (only for heat transport).
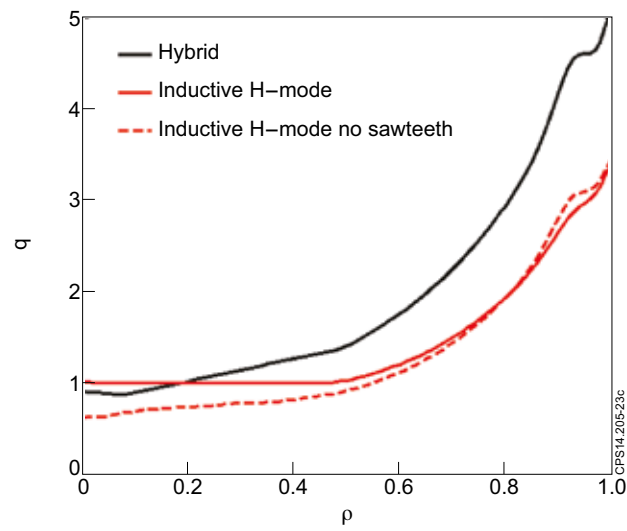
Figure 23: Comparison between the q profiles obtained for the inductive H-mode (with and without sawteeth model) and hybrid JT-60SA scenarios.